

School of Civil & Mechanical Engineering
MXEN4000 - Mechatronic Engineering Research Project 1
Progress Report

Development of an in-situ soil moisture sensor array for real-time soil moisture depth sensing.

Semester 1, 2024

Edward Munns
18871773

Supervisor: Dr Tele Tan

Abstract

Moisture seeking is a crop optimization technique used in agricultural cropping operations where seed is placed at a point in the soil profile with moisture levels high enough for germination and emergence to begin. The technique is commonly used in the agricultural sector but currently requires manual adjustment of equipment to account for changes in soil moisture depth. This work conducted an initial examination into the design of a soil moisture sensor array designed to automate this adjustment process. Testing focussed on the frequency requirements of such a sensor, how a design might conform to the mechanical constraints of the sensing environment, and how sensor characterization might be carried out. A frequency band of 10-100 MHz was identified as suitable for soil moisture sensing, high purity alumina ceramic was identified as a material likely to provide the necessary properties to protect the sensor from the sensing environment, and a method of characterization was presented which demonstrated a linear relationship between the output voltage and permittivity of the test samples.

Table of Contents

Table of Contents	i
Table of Figures	iii
Nomenclature	iv
1. Introduction	1
2. Literature Review	2
3. Background	4
3.1 Crop Establishment and Sowing Time	4
3.3 Nil-till and No-till Sowing Systems	5
3.4 Constraints of the Sensing Environment	6
3.5 Capacitive Sensors in Moisture Sensing	6
4. Aims	11
4.1 Material Analysis for Mechanical Shield	11
4.2 Source Commercially Available Test Sensors	11
4.3 Frequency Analysis of Test Sensors	11
4.4 Evaluate Ability of Test Sensors to Penetrate Mechanical Shield	11
4.5 Develop and Evaluate Sensor Characterization Methodology	11
5. Methodology	12
5.1 Commercial Sensors for Testing	12
5.2 Frequency Analysis	13
5.3 Substrate Penetration	14
5.4 Sensor Characterization	14
6. Results and Discussion	17
6.1 Mechanical shield	17
6.2 Frequency Analysis of IDC and CPC sensors	18
6.3 Substrate Penetration	20
6.4 Characterization of IDC Sensor	22
7. Future Work	24
7.1 Plan of Approach for Future Development	24
7.1 Gantt Chart	25
8. References	26
Appendix A: Coleoptile Length Classification of Certain Wheat Varieties	A
Appendix B: Soil Classification Correlation Matrix	B
Appendix C: Deviation of Method Described by Rego Segunda et al	C
Appendix D: Methylated Spirits Composition and Uncertainty Calculations	D
Appendix E: Complex Permittivity of Ethanol vs Frequency	E

Appendix F: Water Miscibility Chart	F
Appendix G: Dielectric Constant of Common Solvents.....	G

Table of Figures

Figure 1: Wheat seed during germination.....	4
Figure 2: Diagram of "Nill-Till" sowing system..	5
Figure 3: Parallel Plate Capacitor.	6
Figure 4: Electric Field of Parallel Plate Capacitor	6
Figure 5: Transformation from Parallel Plate to Coplanar Capacitor.....	7
Figure 6: Coplanar Capacitor and Coplanar Capacitor with Ground Plane.....	7
Figure 7: Diagram of IDC.....	8
Figure 8: Complex Permittivity as a Function of Frequency.....	9
Figure 9: Radiocontrolli IDC Sensor and Grow CPC Sensor.....	12
Figure 10: Apparatus used for frequency analysis.....	13
Figure 11: Circuit used for frequency analysis.	13
Figure 12: Substrate penetration testing setup.	14
Figure 13: Low pass filter circuit used for sensor characterization	15
Figure 14: Simulation of $V_{out\ pp}$ bounding signals at C_{min} and C_{max} of the IDC Sensor. 16	
Figure 15: Grow CPC Sensor Frequency Plot.	18
Figure 16: Radiocontrolli IDC Sensor Frequency Plot.....	19
Figure 17: Result of IDC Al ₂ O ₃ substrate penetration testing.....	20
Figure 18: Result of CPC Al ₂ O ₃ substrate penetration testing.	21
Figure 19: Radiocontrolli IDC Sensor Characterization Results.	22
Figure 20: Coleoptile length, establishment rate, and yield of a range of wheat varieties at 0, 4 and 10 cm sowing depth.	A
Figure 21: List of wheat varieties and their coleoptile group classifications.	A
Figure 22: Soil Classification Features used for Model Evaluation..	B
Figure 23: Correlation Matrix of Soil Parameters..	B
Figure 24: Methylated Spirits Composition.....	D
Figure 25: Relative Permittivity Values used for Characterization..	D
Figure 26: Complex Permittivity of Ethanol vs Frequency..	E
Figure 27: Water Miscibility Chart.....	F
Figure 28: Permittivity of Common Solvents.....	G

Nomenclature

Symbols	Definition	SI unit
V	Voltage	Volt
V_{pp}	Peak to peak voltage	Volt
Q	Electric charge	Coulomb
f	Frequency	Hertz
f_{cutoff}	Cut-off frequency	Hertz
ω	Angular frequency	Radians/second
R	Resistance	Ohms
C	Capacitance	farad
j	Imaginary unit	-
ϵ_0	Permittivity of free space, 8.854×10^{-12}	farads/meter
ϵ	Absolute complex permittivity	farads/meter
ϵ'	Real component of ϵ	-
ϵ''	Imaginary component of ϵ	-
ϵ_r	Relative complex permittivity	-
ϵ_r'	Real component of ϵ_r	-
ϵ_r''	Imaginary component of ϵ_r	-
Δ	Change in	-

Abbreviations	Definition
MUT	Material under test
DUT	Device under test
PCB	Printed circuit board
FDR	Frequency domain reflectometry
PPC	Parallel plate capacitor
CPC	Coplanar capacitor
IDC	Inter-digital capacitor
DMM	Digital multi-meter
AC	Alternating current

1. Introduction

In recent years, progress in the fields of electronics miniaturization, data processing, wireless transmission, and machine learning have led to the development of entirely new sensor technologies and sensing domains. In some cases, these advances have enabled the collection of previously inaccessible environmental datasets which have the potential to improve economic and environmental outcomes for stakeholders and industry. With many outcomes dependant on environmental conditions, agriculture is one sector which could benefit greatly from these advances.

The application of sensing and actuation systems has historically seen widespread adoption in the Australian agricultural sector. Mechanization of the sector over the last century saw the introduction of machinery targeted at agricultural tasks. Integration of sensing and compute systems into agricultural machines has enabled precision farming techniques like yield mapping and fertilizer rate control to be used to further optimize outcomes and guide the decision-making process. The ability to gather data in real-time of environmental factors like rainfall, temperature, and soil moisture is likely to be a key driver of future development in the industry.

A critical application of soil moisture sensing for cereal crop producers occurs during the sowing period, when a method known as moisture seeking is employed to optimize crop establishment. In moisture seeking, sowing depth is adjusted to place seed at a layer in the soil with enough moisture to enable germination. A real-time sowing depth control system could vastly improve the outcomes of this process and lead to crop yield increases for stakeholders in the agricultural sector. This research focusses on the design of a novel soil moisture sensor array for use in the feedback loop of such a system.

2. Literature Review

This research began with an in-depth review of the current literature. The purpose of this review was to establish the current state and trends of soil moisture sensing, to identify technologies applicable to the real-time, in-situ requirements of this application, and to identify related works this research could build upon.

Yu et al published a review of soil moisture sensing technologies and research in 2021. In this review weight, tensiometer, neutron probe, gamma-ray, infra-red, and dielectric soil moisture sensing methodologies were examined. A summary of the major findings of previous studies into many commercially available sensors was included in this review. Capacitive sensors were identified as providing major cost benefits over time domain reflectometry devices, but the review also highlighted the importance of correction algorithm optimization in providing accurate measurements. Factors affecting accuracy of capacitive sensors identified include installation method, temperature drift, soil type, ionic conductivity and unoptimized or inappropriate algorithms (Yu, et al. 2021).

Escriba et al developed a co-planar soil sensor capable of sensing both soil salinity at lower frequency (300-1000 kHz) and soil moisture at higher frequency (4-10 MHz) by switching of the oscillation sources providing excitation to the sensor. This design was based on a traditional co-planar capacitor (CPC) design with electrodes arranged in a novel double helix layout. Results showed dissolved Ionics present in the material under test (MUT) lead to high variability of moisture readings at lower frequencies with these readings converging at higher frequencies. This work also examined the effects of including a polymer layer encasing the sensor to provide mechanical shielding. This shielding demonstrated a constant increase in measured capacitance across the 10-60% soil moisture range of an estimated 14.7pF and an overall reduction in sensor sensitivity of 12% due to the additional parasitic capacitance introduced by this layer (Escriba, et al. 2020).

Claudel et al presented an analytical method for optimization of interdigital capacitive (IDC) sensors. Results of this method were validated against finite element analysis simulations. This study demonstrated penetration depth and bandwidth were largely dependent upon electrode and inter-electrode gap widths (Claudel, et al. 2021).

Patle et al developed a sensor array consisting of 5 sensors placed at 5 cm increments over a 25 cm soil depth profile. These sensors were IDCs constructed on a 2-layer PCB with the IDC electrodes mirrored on both sides of the PCB. This mirroring of the electrodes demonstrated a tripling of capacitance compared to earlier works with an average ΔC of 300pF across the 5 sensors. The design used time domain multiplexing to iterate through all sensors in the array over a 250ms period with output signals feed into a counter to convert capacitance to pulse rate (Patle, et al. 2022).

Kim, Chae and Nishigaki developed a method of compensating for air content present in soil pores using ethanol injection. This ethanol displaced air in samples and FDR measurements were taken at a frequency of 1 GHz. The method presented allows for the estimation of effective and physical porosities in saturated soils by calculation of total permittivity estimates from known permittivity values of soil component materials and the ratios of these materials in the sample (Kim, Chae and Nishigaki 2008).

Finlay and Howard iteratively developed prototypes of 1, 3, and 36 row crop sowing machines featuring a semi-autonomous real-time depth control system implemented with hydraulic actuators and using an array of soil moisture sensors to provide system feedback. Field trials were performed across multiple growing seasons beginning with the single tine prototype. This design was trailer mounted and towed by a utility vehicle. The trial tested various sensor types and helped to refine the hydraulic control system. A major limitation of this trial was that the single row rendered concurrent testing of multiple sensors impossible. The 3-tine prototype was mounted on a small agricultural tractor. In this trial the hydraulic system was supplied by the tractor. The higher tine count allowed for concurrent testing of multiple sensors but increased the actuation system complexity significantly as actuators also had to be controlled concurrently. Pressure and load sensors were incorporated to provide data of forces in tines at variable tillage depths. The latest trial occurred in 2023 with the 36-row design. The 36 sowing tines were mounted on a 12-meter frame for full-scale testing of the system. The parallel compute requirements due to the high tine count made control software a challenge. Objectives of the project in 2024 include implementing system control over ISOBUS, further in-field trials and the development of a new sensor to improve accuracy and wear resistance (Finlay and Howard 2024).

Sulek and Ogorkiewicz analysed the effects of sowing depth and seed size on germination quality and harvest yield of wheat plants. Sowing depths of 1 cm, 3 cm, 5 cm, and 7 cm and seed size classes of small (1.8-2.2 mm), medium (2.2-2.5 mm), and large (>2.5 mm) were evaluated on germination time and germination percentage. Results showed higher germination rates with the large seed group, the 5 cm and 7 cm deep sowing delayed germination and reduced germination rate, and the optimal group was the large seed with 3 cm sowing depth (Sulek and Ogorkiewicz 2020).

Rego Segundo et al presented a method of approximating complex permittivity using a current-to-voltage conversion circuit and dual frequency amplitude measurement. This method had the benefit of not requiring phase measurement of signals, leading to lower component speed requirements and lower complexity of circuits compared to the traditional method of measuring both amplitude and phase of signals. Results demonstrated maximum error of 0.6% for electrical conductivity measurement and maximum error of 2% for relative permittivity measurement (Rêgo Segundo, et al. 2019).

With a low cost of construction, real-time sensing capability, and no requirement for direct contact between sensing electrodes and the MUT, capacitive frequency domain reflectometry was identified as an applicable sensing pathway. The review identified co-planar capacitor designs used in FDR sensors could be classified into CPC and IDC designs. The method of switching sensing domains from ionic to dipolar presented by Escriba et al could enable real-time measurement of both permittivity and ionic characteristics of a soil profile with the type of sensor array proposed for this work. Finally, the method of complex permittivity characterization presented by Rego Segundo et al was recognized as an approach which could benefit the accuracy and economics of a sensor array design.

3. Background

3.1 Crop Establishment and Sowing Time

Sowing time and quality of seedling establishment have a large influence on the yield outcomes of cereal crops and is a critical decision-making point in a season for agricultural business. Seed can be wet sown, where it will begin growing immediately, or dry sown, where it will lay dormant in the soil until a rainfall event. Wet sowing refers to placing the seed at a depth in the soil profile with enough moisture to begin germination, it can still be performed when the surface layers of the soil are dry. Sowing using this method can accelerate emergence times (GDRC 2016), lead to better establishment rates and provide better control of weed species from knockdown and pre-emergent herbicide applications. With the large scale of many Australian cropping operations, it is often not possible to use this method over an entire program, and waiting for rain before sowing is often not an option. To cover the large areas involved, dry sowing a percentage of a cropping program with long season cereal varieties is a common practice. These crops will begin growing with the opening rains of a season, but these areas must be prepared in advance to ensure weed seed burdens are low as the use of knockdown herbicides is not possible (Congreve 2022).

Seed will start germinating when 35-45% of its dry weight in moisture has been absorbed. Proteins and starch in the seed are converted by enzymes into sugars for energy, and the radicle, seminal roots and coleoptile emerge from the seed (GDRC 2016). The coleoptile is vital to the successful emergence of the seedling. This structure encases the first leaves to protect them from damage, it elongates as it pushes through the soil and guiding them to the surface. On reaching the surface the leaves emerge from the tip of the coleoptile and the seedling can begin acquiring energy through photosynthesis (Oregon State University 2024).

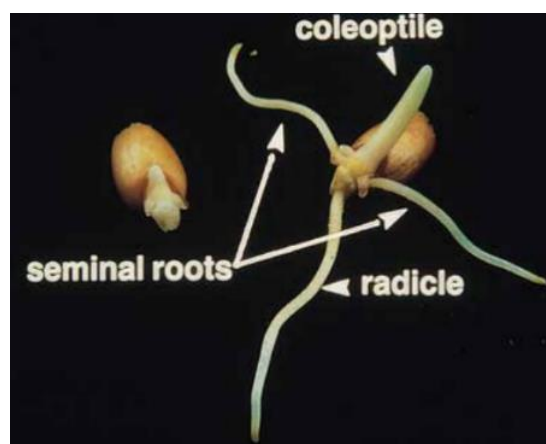


Figure 1: Wheat seed during germination. From: (GDRC 2016).

Seed size can have a large impact on the success of crop emergence. Until photosynthesis begins, the only energy the seedling can access comes from the seed. Zareian et al compared sizes of wheat seeds for germination and emergence rates. They found that although seed size had little impact on germination, it had a large impact on emergence rates, with the 2-2.2 mm seed group having an emergence rate of 67.95% compared to the 2.8-3 mm group at 80.55% (Zareian, et al. 2013).

The coleoptile length of a cereal crop species can vary greatly between varieties and is a major factor in the ability of seed to emerge for depth. Pampa et al suggest a sowing depth which exceeds the coleoptile length of the variety can result in poor crop establishment due to shoots emerging from coleoptile below the ground surface (Pampa, et al. 2013). Appendix A shows a table of wheat varieties and the results from a 2021 field trial which compared coleoptile length, sowing depth, and yield of several wheat varieties.

3.2 Moisture Seeking to Optimize Crop Emergence

Moisture seeking refers to the implementation of strategies to conserve pre-sowing soil moisture allowing crops to be wet sown into a layer of the soil profile where the germination and emergence process will begin straight after sowing. Strategies to conserve soil moisture include minimizing soil tillage to avoid losses from evaporation and removing weed species over the summer period with knockdown herbicides. During planting, sowing depth is adjusted to place seed at a high moisture point in the soil profile. Recent wheat breeding research conducted by the CSIRO has focussed on creating longer coleoptile crop varieties capable of emerging from deeper in the soil profile. Field trials on two new wheat varieties (Mac and Mace 18) successfully emerged from a sowing depth of 120 mm (GRDC 2024). Commercial release of varieties with these traits could vastly increase the opportunity for growers to take advantage of moisture seeking practices to optimize crop yields.

3.3 Nil-till and No-till Sowing Systems

The dominant broad-acre crop sowing method in Australia is based on a system referred to in the industry as “nil-till” or “no-till”, with 74% of Australian cereal crops sown using this method as of 2016 (Llewellyn and Ouzman 2020). This system has largely replaced traditional aggressive tillage methods, where tillage points were designed to till wide and shallow to remove weed plants in front of seed placement. In contrast, the nil-till system uses long (150-250 mm), thin (~15 mm) tillage points to penetrate soil layers below the sowing depth (Ausplow 2024). The major benefits of this system over the traditional method are to allow fertilizer to be placed below the seed bed so plant roots can grow into this fertilized zone, to minimize the loss of soil moisture caused by the tilling process, and to optimize the outcomes of Trifluralin based pre-emergent herbicide application.

Figure 2 shows an implementation of a nil-till sowing system. The tilling point cuts a narrow, deep slot into the soil profile. Behind the tilling point is a fertilizer dropper where solid or liquid fertilizers are dropped into the slot at depth and soil is then allowed to backfill the slot. Next, the opening tool re-opens the top portion of the slot at a pre-set sowing depth and seed is placed at this depth through a seed dropper. Sowing depth can be adjusted by vertical adjustment of this opening tool; however, this cannot be done in real-time as it requires the adjustment of mechanical fasteners as illustrated by the 2 adjustment bolts in figure 2. Finally, a press wheel compresses the soil directly over the seed. Changes in local soil height are compensated for by connecting the entire seed placement assembly to the main assembly through a spring-loaded hinge which rides on the press wheel as

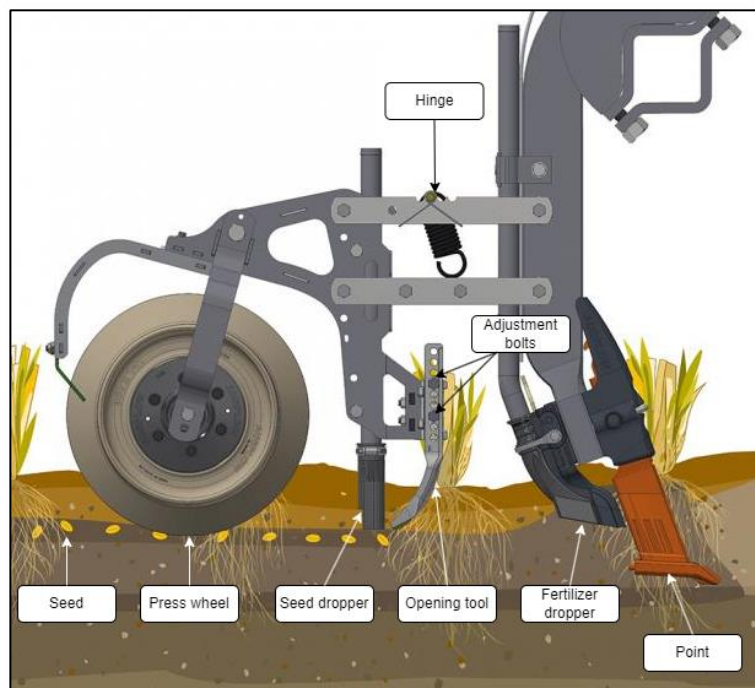


Figure 2: Diagram of "Nill-Till" sowing system. From: (Ausplow 2024).

the local soil height changes.

3.4 Constraints of the Sensing Environment

The sensing environment of this application presents significant design challenges. The sensor array must be located below the soil surface in contact with the soil between the point and the opening tool in figure 2 to provide the required readings. This environment is extremely abrasive, mechanically aggressive, and crop fertilizers being applied to this zone can be highly corrosive. A successful design must be capable of accurate and reliable measurement while providing an acceptable operational lifetime in this environment and being economically viable.

3.5 Capacitive Sensors in Moisture Sensing

In electrical circuits, a capacitor is a component which can store electrical energy over time. The most common type of capacitor is the parallel plate capacitor (PPC), where electrodes are conductive plates on parallel planes with area A , separated by a dielectric of thickness d and permittivity ϵ (figure 3). A voltage at the plates causes the charges $+Q$ and $-Q$ to accumulate opposing charges in the dielectric at the surface of the plates. This polarization generates an electric field in the dielectric. Capacitance is a measure of the ability of a capacitor to store electric charge:

$$C = \frac{Q}{V} \quad (1)$$

Which for a PPC can be approximated by:

$$C = \epsilon \frac{A}{d} = \epsilon_0 \epsilon_r \frac{A}{d} \quad (2)$$

This approximation requires that d is small and is uniform at every point over the area A . This simplifies the above calculation by allowing the electric field to be treated as a uniform electric field with force vectors perpendicular to the plate surfaces at all points of A . In this case, the force vectors which extend out beyond the edge of the plates (figure 4) can be considered insignificant. This protrusion of the field from the edges of the capacitor is known as a fringing field.

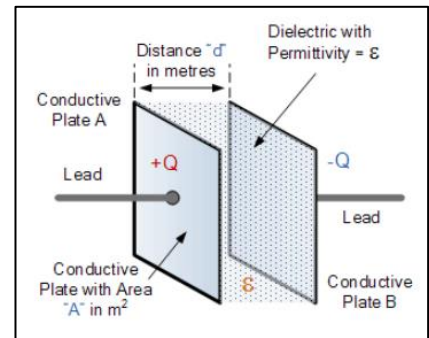


Figure 3: Parallel Plate Capacitor
From: (Electronics Tutorials 2024).

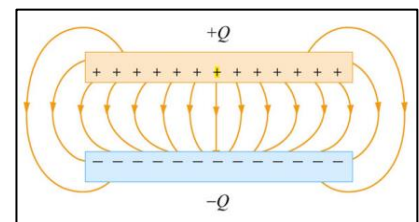


Figure 4: Electric Field of Parallel Plate Capacitor From: (MIT n.d.)

For sensing applications, the dielectric of a capacitor is replaced with the MUT and a $\Delta\epsilon$ of the MUT results in a ΔC of the capacitor. A PPC arrangement requires the MUT to be placed between the electrodes which limits the sensing domains of PPC sensors. CPCs overcome this limitation by rearranging the plates from a parallel (Figure 5, Left) to a coplanar layout (Figure 5, Right).

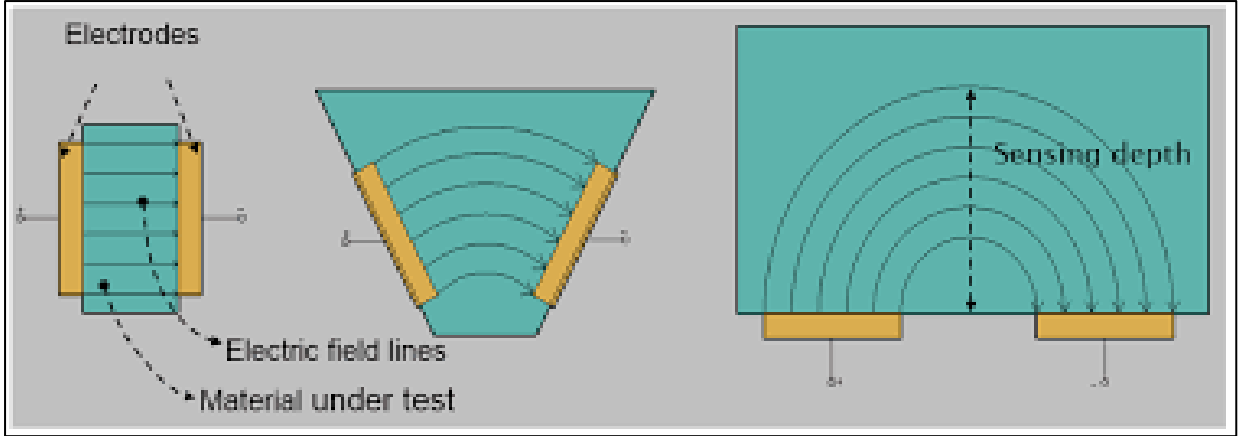


Figure 5: Transformation from Parallel Plate (Left) to Coplanar (Right) Capacitor From: (Yang, et al. 2015).

This change also transforms the electric field from being primarily uniform to being primarily a fringing field. Switching to a fringing field makes the modelling of CPC capacitance a greater challenge compared to the PPC case. The geometric parameters of a CPC are the electrode width w , the gap width g , the electrode length L , the electrode height h , and the depth of the field T . Claudel et al suggest the following model can reliably approximate CPC capacitance, providing $L \gg w$ and $\frac{w}{g} \gg 1$ (Claudel, et al. 2021):

$$C = \frac{2\epsilon_0\epsilon_r L}{\pi} \ln \left[\sqrt{\left(1 + \frac{2w}{g}\right)^2 - 1} + \left(1 + \frac{2w}{g}\right) \right] \quad (3)$$

Important factors for CPC designs are the minimisation of parasitic capacitance and directing of the fringing field. The electrode height h creates a PPC-like arrangement across the gap between the electrodes. Minimizing h results in a minimal value of A in equation 2, which minimizes this parasitic capacitance. Figure 6 demonstrates the use of ground planes for directing the fringing field into the MUT. The CPC with no ground plane (Figure 6, left) emits fields from both sides of the electrodes. If the intention of such a design is for the MUT to be placed only on one side of the sensor, a large percentage of the total field is not in the MUT, only contributing noise to the output signal. By placing a ground plane below the excitation electrode (Figure 6, right) the noise in the output signal is replaced with a constant parasitic capacitance through the substrate.

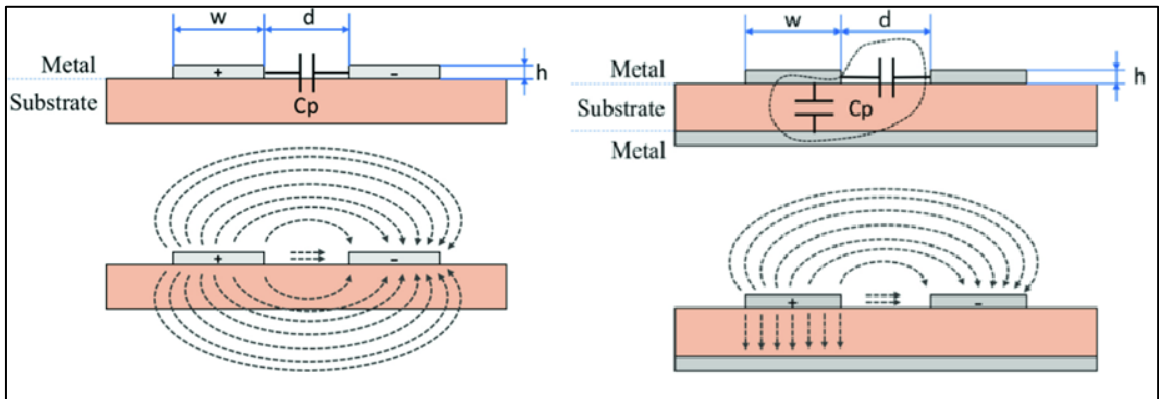


Figure 6: Coplanar Capacitor (Left) and Coplanar Capacitor with Ground Plane (Right) From: (Bodini, et al. 2018).

The method presented by Patle et al of mirroring electrodes of the same charge on both sides of a PCB is a more optimized field directing technique which can be implemented in double

sided sensing applications. Excitation electrodes with are mirrored on both sides of the PCB and the repulsive force between them eliminates the parasitic capacitance in the substrate and directs the fields into the MUT on either side. Patle et al demonstrated a tripling of usable capacitance with this method in a comparison with earlier works (Patle, et al. 2022).

IDC sensors are a subset of CPC sensors with electrodes consisting of sets of interleaved fingers (figure 7). By surrounding the perimeter of fingers of one electrode with those of the other, IDCs can have advantages over CPCs. This arrangement can provide much higher capacitance for a given area. The geometric parameters of gap width, electrode width, and periodicity λ can also be tuned to optimize the field penetration depth.

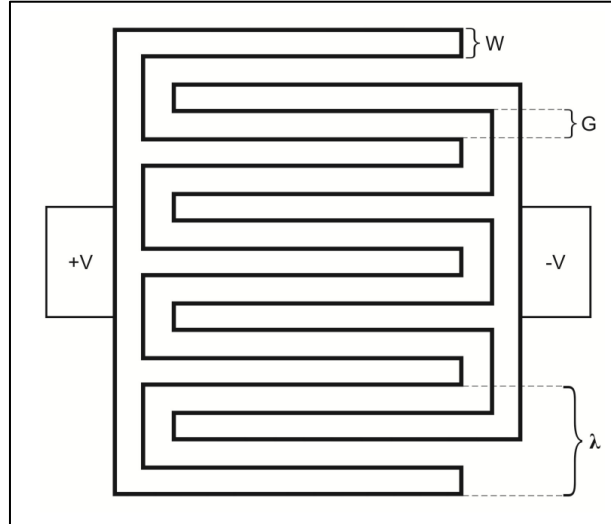


Figure 7: Diagram of IDC. From: (González, et al. 2015).

3.6 Challenges in Soil Moisture Sensing

Capacitive soil moisture sensors are normally required to be calibrated to suit the soil at the installation site to provide accurate output. This project requires calibration to be performed autonomously in real-time. Soil parameters such as clay content, ionic content, conductivity, pH, carbon content, void density, and texture can change over short distances and the permittivity of the MUT will change with these factors. This will require advanced control system algorithms to be implemented in the future, but in the design phase of the project it is critical that as much reliable data can be provided from the sensor array as possible.

For materials with isotropic dielectric properties, ϵ is a complex number (Li, Wu and Shen 2022) with real and imaginary components:

$$\epsilon = \epsilon' - j\epsilon'' \quad (4)$$

$$\text{where } j = \sqrt{-1} \quad (5)$$

ϵ is also frequency dependant and can be represented as a function of the angular frequency ω of the input signal:

$$\epsilon(\omega) = \epsilon'(\omega) - j\epsilon''(\omega) \quad (6)$$

$$\text{where } \omega = 2\pi f \quad (7)$$

Figure 8 from Li et al shows the magnitudes of the ϵ' and ϵ'' components of ϵ as function of frequency.

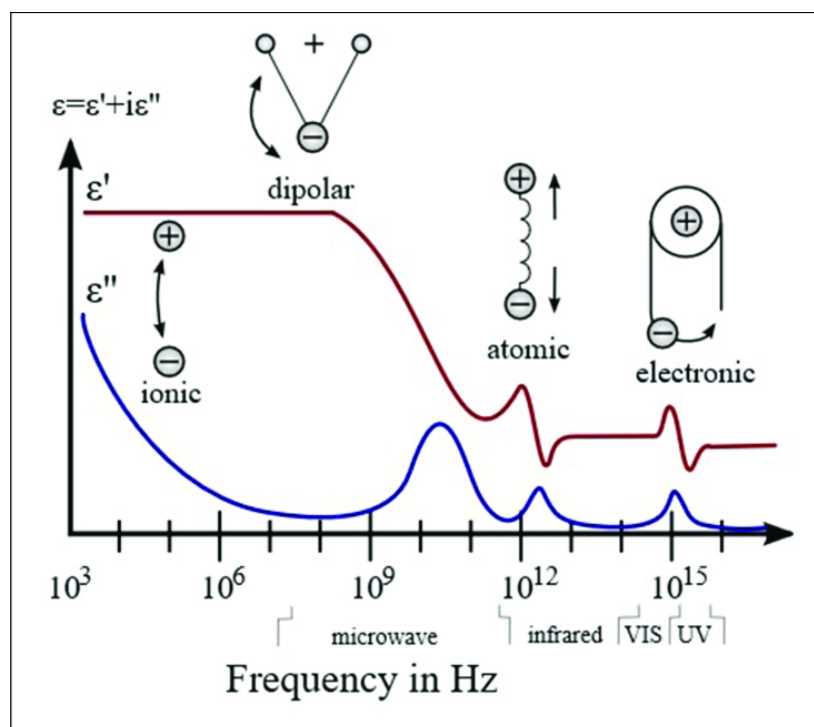


Figure 8: Complex Permittivity as a Function of Frequency. From: (Li, et al. 2019).

The complex permittivity can be used to classify the field propagation and dielectric properties of materials:

$$\text{Dielectric Class}(\epsilon) = \begin{cases} \text{Lossless, perfect dielectric, } \epsilon''/\epsilon' = 0 \\ \text{Low - loss, good dielectric, } \epsilon''/\epsilon' \ll 1 \\ \text{Lossy propergation medium, } \epsilon''/\epsilon' \approx 1 \\ \text{High - loss, poor dielectric, } \epsilon''/\epsilon' \gg 1 \\ \text{Perfect conductor, } \epsilon''/\epsilon' \rightarrow \infty \end{cases} \quad (8)$$

The method proposed by Rego Segundo et al suggests the following approach for real-time measurement of complex permittivity. For sub-GHz excitation frequencies, relaxation effects of the real component of complex permittivity can be neglected (as seen in figure 8) and ϵ_r can be modelled as:

$$\epsilon_r = \epsilon_r' - j \frac{\sigma}{\omega \epsilon_0} \quad (9)$$

Where σ is the electric conductivity in siemens per meter (Rêgo Segundo, et al. 2019), and the complex admittance Y can be approximated with:

$$Y = j\omega k_g \epsilon_0 \epsilon_r \quad (10)$$

Where k_g is the geometric configuration constant of the sensor (Rêgo Segundo, et al. 2019), i.e. for the simple PPC case in equation 2, $k_g = \frac{A}{d}$. A full derivation of this method can be seen in Appendix B.

This method uses a similar dual frequency approach to the one presented by Escriba et al to measure conductivity at a lower frequency and permittivity at a higher frequency, enabling both components of the complex permittivity to be characterized without the need for the high-speed circuits required for phase measurement. It is highly likely a characterization of both components would greatly improve the soil type classification outcomes of a control system for this work.

4. Aims

4.1 Material Analysis for Mechanical Shield

To provide functionality in the sensing environment and an economically viable operational lifetime, the sensing elements of the sensor array must be protected from mechanical wear and impact. This will require a mechanical shield layer to be placed between the sensing elements and the MUT. This shield must be capable of withstanding the highly abrasive, mechanically aggressive, and corrosive sensing environment. When sensing, the fringing field of sensors must be capable of penetrating the shield into the MUT. This requirement places additional constraints on the electric and dielectric properties of the shield. A suitable material must be identified with properties that satisfy these requirements while being economic viable for this use-case.

4.2 Source Commercially Available Test Sensors

The literature review identified CPC and IDC designs were used for soil moisture applications, but a direct comparison between them was not found. Commercially available sensors of both CPC and IDC designs must be sourced for experimental comparison.

4.3 Frequency Analysis of Test Sensors

The influence of ϵ_r' and ϵ_r'' on the change in capacitance of a capacitive sensor are frequency dependant. High level analysis of relationships between frequency dependant variables can be performed via visual inspection of a Bode plot showing the magnitude and phase of the frequency response of the system. A frequency analysis should be carried out on the test sensors to guide excitation frequency decisions of a design.

4.4 Evaluate Ability of Test Sensors to Penetrate Mechanical Shield

Once a suitable shield material has been identified and sourced, an experiment must be designed to assess the ability of the test sensors to deal with the constraints introduced by the shield layer.

4.5 Develop and Evaluate Sensor Characterization Methodology

A full characterization of a sensor array for this application will likely require the examination of many variables. Developing and evaluating an initial characterization method could highlight aspects of the experimental process that require refinement. A trial run of characterization should be carried out on the test sensors.

5. Methodology

5.1 Commercial Sensors for Testing

To guide the design of an application specific sensor for this project, two commercially available moisture sensors were sourced. The first sensor was a Radiocontrolli RC-SPC1K capacitive rain sensor featuring a high digit count, low digit width IDC sensing element on one face of a thick-film substrate of alumina. The sensing element is covered with a thin blue polymer layer which keeps the sensing element electrically isolated from the MUT. The data sheet states a minimum capacitance of 100pF when completely dry and a maximum capacitance of >550 when completely wet (Radiocontrolli n.d.). Although this sensor was designed to measure rain, output depends on permittivity of the sample, thus it can also function as a soil moisture sensor. The primary reasons for selecting this sensor for testing were the IDC layout, high capacitance, and thick-film ceramic construction. The sensor was waterproofed to enable complete submersion in liquid samples by 3D printing a small mounting frame and filling the frame with epoxy resin.

The second sensor was a Grow Soil Moisture Sensor featuring dual CPC sensing elements constructed on the inner 2 layers of a 4-layer FR4 PCB. The sensor uses a 555-timer IC to generate the excitation signal and outputs a frequency which varies with ϵ of the MUT. The 555-timer circuit was disconnected from the sensing elements by severing the PCB traces so input and output signal wires could be soldered directly to the element pads. The construction technique of this sensor ensures the sensing elements are electrically isolated from the MUT, so no further waterproofing was required.

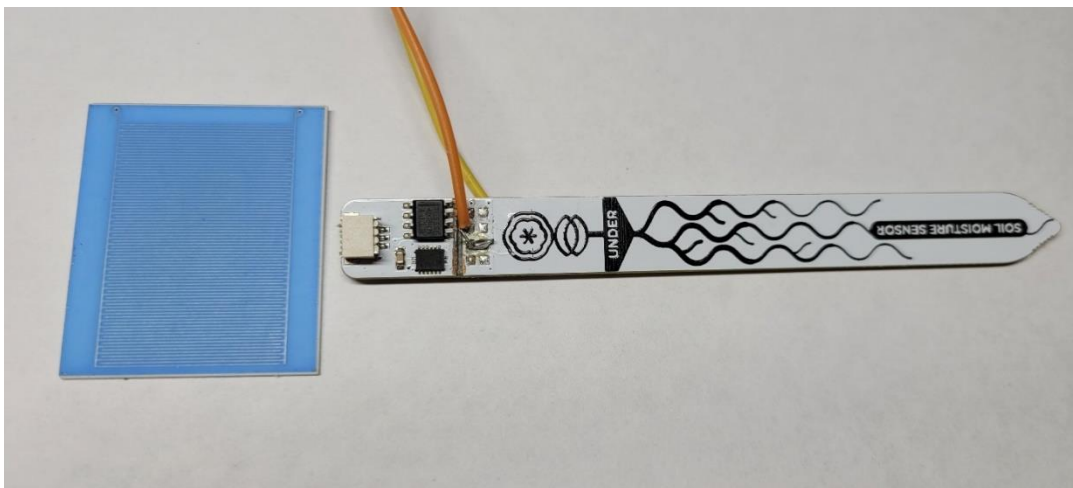


Figure 9: Radiocontrolli IDC Sensor (left) and Grow CPC Sensor (right).

5.2 Frequency Analysis

Frequency analysis was performed on both sensors to visualize the effects of ϵ_r' and ϵ_r'' over a bandwidth of 1kHz to 120MHz. A Siglent SDS1204 X-E 200MHz oscilloscope and SDG2122X 120MHz signal generator were connected over USB to allow NI-VISA commands sent from the oscilloscope to control the generator. 50 Ω coaxial cables of equal length were connected from both outputs of the generator to a multi-channel SMA test fixture with the configuration seen in figure 11. Two 50 Ω feed-through terminations were used at oscilloscope inputs 1 and 3 to match the input impedance of the generator. Channel 2 of the signal generator was then slaved to channel 1 and the Bode plot function was setup for a frequency sweep from 1kHz to 120MHz with a 1 V_{pp} AC sin wave input. This configuration uses the input at channel 1 of the oscilloscope as a reference signal to generate the magnitude and phase plots of the input on channel 3.

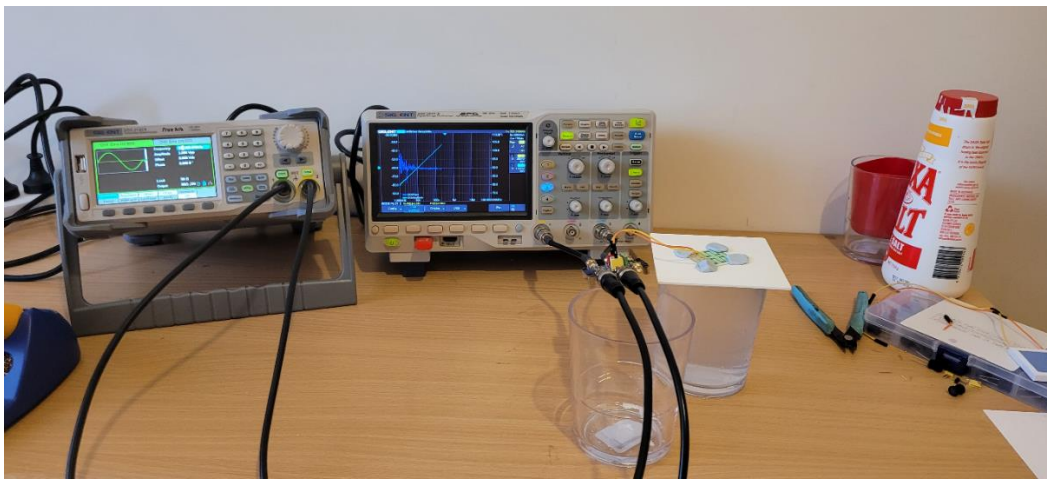


Figure 10: Apparatus used for frequency analysis.

In the circuit used for frequency analysis the capacitive sensor and the 50 Ohm termination resistor form an RC high pass filter. The cut-off frequency f_{cutoff} of this filter varies with ΔC of the sensor, which in turn varies with $\Delta\epsilon$ of the MUT.

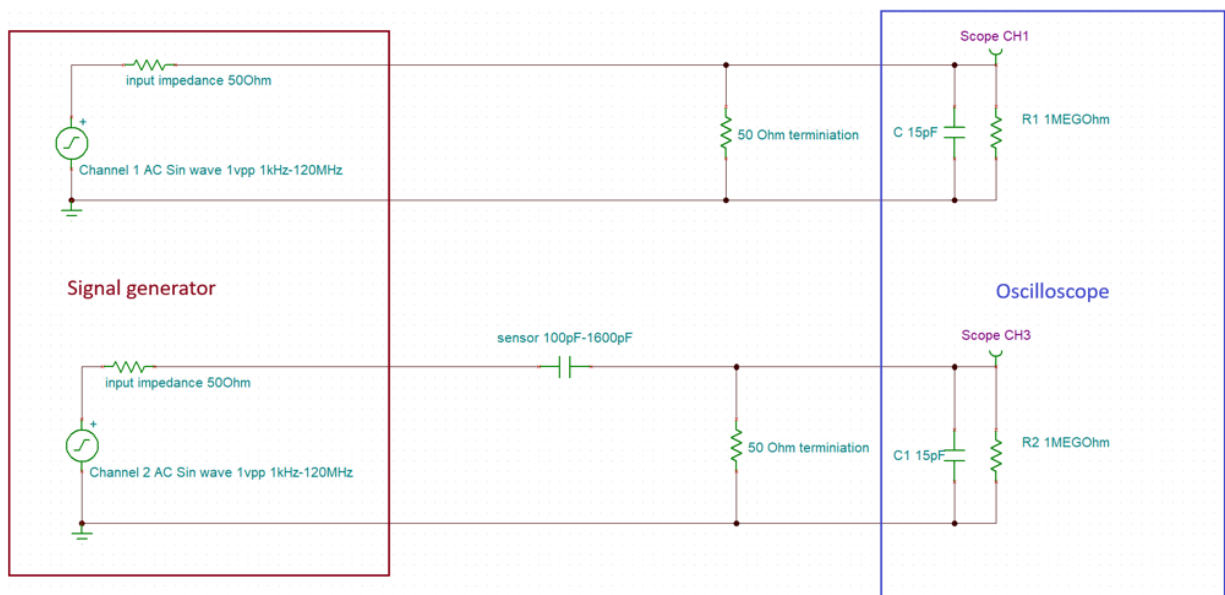


Figure 11: Circuit used for frequency analysis.

Frequency analysis examined the effects of both the change in the relative permittivity and the change in the ionic content by combining the data from the same test performed on 2 separate test groups. To examine the frequency response over a range of ϵ_r values, samples of distilled water ($\epsilon_r \approx 80$), methylated spirits ($\epsilon_r \approx 25$), canola oil ($\epsilon_r \approx 3$) and air ($\epsilon_r \approx 1$) were measured. This group is collectively referred to as the permittivity group. The ionic effects were examined using solutions of distilled water and 0.25%, 0.5%, 1% and 1.5% NaCl by volume, this group is collectively referred to as the ionic group.

5.3 Substrate Penetration

To assess the ability of the sensors to penetrate the mechanical shield the sensors were attached to a 96% pure Al_2O_3 substrate of 1mm thickness with the sensing element face down. Substrates were then slid through the meniscus of distilled water samples filled above the rim of the sample cup, so the bottom face of the substrate was in contact with the sample. The frequency sweep process was then repeated in this configuration and results were plotted against the previous readings for air and distilled water submersion.

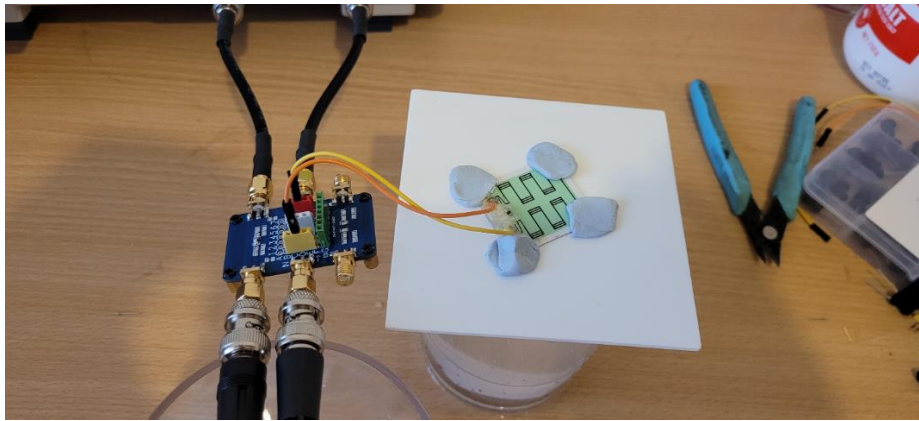


Figure 12: Substrate penetration testing setup.

5.4 Sensor Characterization

Soil moisture measurement is a function of many different variables including temperature, soil conductivity, soil clay content, soil matrix density and organic carbon content among others. A full characterization of a sensor requires each of these variables to be characterized in isolation. The IDC sensor was characterized directly on the variable being measured, the relationship between ϵ of the sample and $V_{out\ pp}$. The focus of this testing was on evaluating the experimental method being used, not on producing a highly accurate sensor model. The method contains several known sources of error which were assumed to have negligible impact on evaluating the methodology. Sensors were submerged in solutions of distilled water and methylated spirits mixed at variable ratios from 100% distilled water to 100% methylated spirits. The methylated spirits used for this testing consists of $\geq 95\%$ ethanol with the remainder consisting of $\leq 5\%$ water and denaturant additives of $< 0.001\%$ Denatonium Benzoate, 0.25% Methyl Isobutyl Ketone, and $< 0.001\%$ Fluorescein (RecoChem 2022).

Relative permittivity values for ethanol and water of 24.6 and 80.4 respectively were used to calculate the estimated permittivity values from the ratio of solutions. It was assumed the denaturant additives would have little impact on results as they are only present in trace amounts. The uncertainty of the methylated spirits was calculated based on the water content, resulting in an ϵ_r value for methylated spirits of $25.6 \pm 5.47\%$ (see Appendix D).

Calculated Permittivity of Characterization Samples			
% Methylated Spirits	% Water	Calculated ϵ_r	Absolute Uncertainty of ϵ_r
0	100	80.4	0
10	90	74.92	0.140032
20	80	69.44	0.280064
30	70	63.96	0.420096
40	60	58.48	0.560128
50	50	53	0.70016
60	40	47.52	0.840192
70	30	42.04	0.980224
80	20	36.56	1.120256
90	10	31.08	1.260288
100	0	25.6	1.40032

Table 1: Calculation of Sample Permittivity for Sensor Characterization.

Fernandez et al suggest the effect of frequency on ϵ_r for water is minimal below 1 GHz (Fernandez, et al. 1995) and Arcone et al suggest the same is true for ethanol in the 10-100MHz band (Arcone, et al. 2008) (see Appendix E). It was therefore assumed that at these frequencies the values calculated above were appropriate for method evaluation. Testing was conducted at room temperature of approximately 22°C.

The circuit used for sensor characterization forms an RC low pass filter with the sensing capacitor and the 50 Ω input impedance. An excitation signal was a 1 V_{pp} AC sin wave set at a constant frequency was used for the excitation signal. This frequency was selected by running a Bode plot simulation in Tina-TI at the upper and lower bounds of sensor capacitance and selecting a frequency with an appropriate $\Delta V_{out pp}$. A frequency of 10MHz was selected to characterize the IDC sensor.

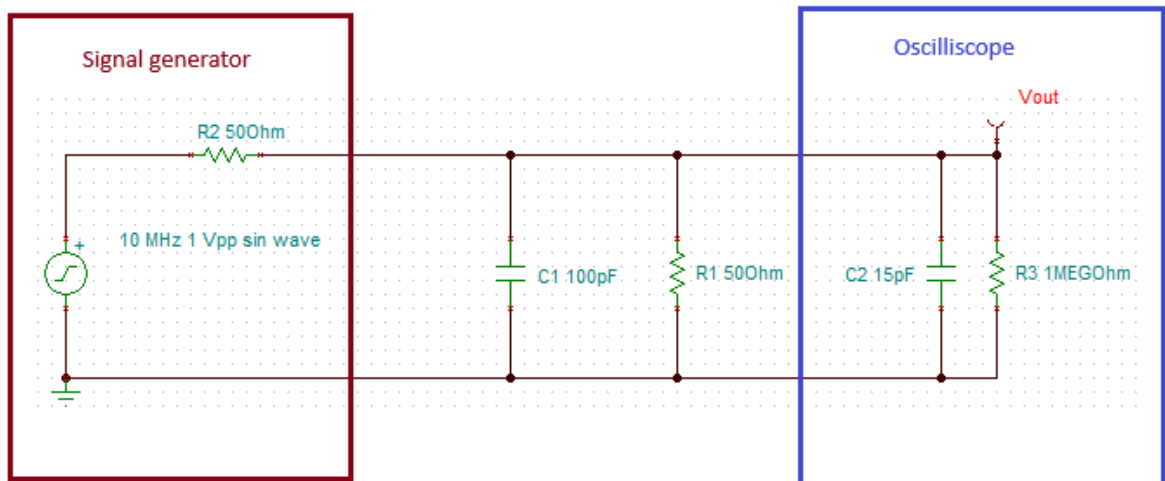


Figure 13: Low pass filter circuit used for sensor characterization

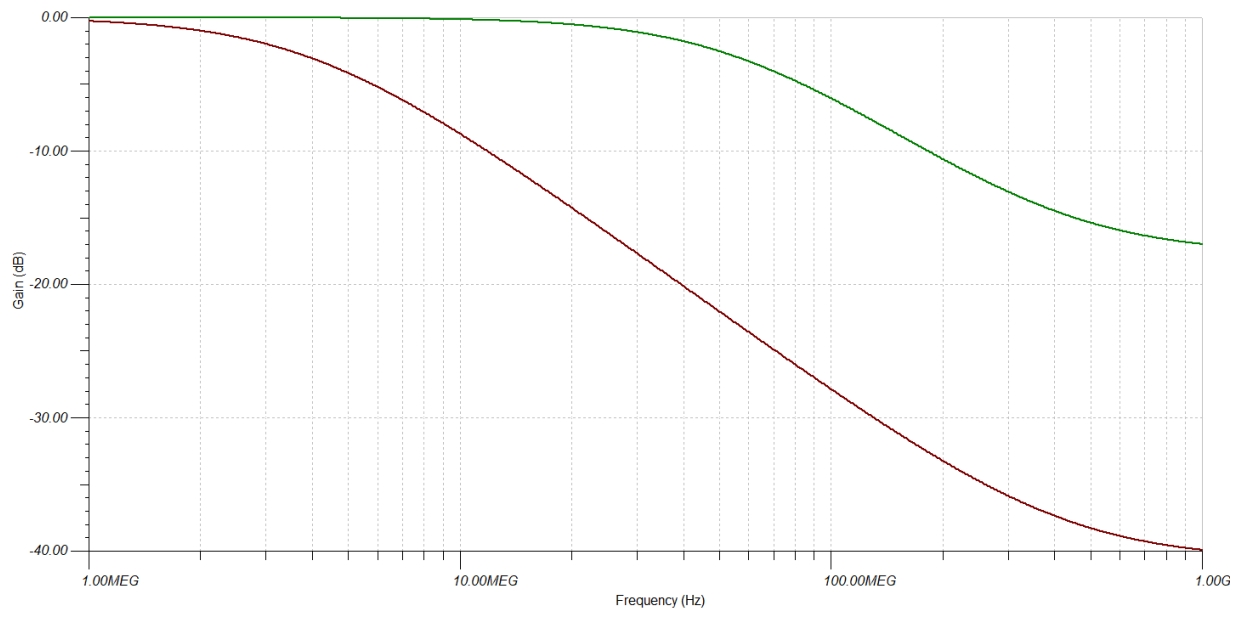


Figure 14: Simulation of $V_{out\ pp}$ bounding signals at C_{min} and C_{max} of the IDC Sensor.

6. Results and Discussion

6.1 Mechanical shield

The shield material cannot be metallic as fringing fields would be negated by a metal. Polymers are commonly used for shielding of sensing elements in soil moisture applications, as was the case in Escriba et al, but it is likely a polymer would not provide the wear resistance this use-case demands. This left ceramics as the most likely material class of material to satisfy the design requirements. Research into the properties of suitable ceramics identified high purity alumina (HPA) as a material likely to be capable of meeting the electrical, mechanical, and economic requirements of the shield layer. HPA ceramic is highly resistant to mechanical wear, finding widespread industrial use in wear plate and liner applications (China Alumina Ceramic 2022). The following relationships between critical properties and alumina purity were identified:

1. Hardness increases with purity
2. Fracture toughness increases with purity
3. Compressive strength increases with purity
4. Loss tangent decreases with purity

These properties all exhibit desirable changes with an increase in the alumina purity of the ceramic. This alumina purity should therefore be maximized (Accuratus 2013).

Two PCB manufacturing techniques that may be applicable to the commercial production of this type of sensor array were also identified during this research. Low-Temperature Co-fired Ceramic (LTCC) is a PCB manufacturing process implemented by stacking layers of HPA impregnated film and conductive trace layers of copper, silver, gold, or platinum. The stack is then sintered at 850-900°C. This process results in boards with high conductivity and excellent high frequency performance. High-Temperature Co-fired Ceramic (HTCC) employs the same process as LTCC, except the sintering temperature is increased to 1500-1800°C and the conductive layers are replaced with a refractory metal such as tungsten or molybdenum. Refractory metals are required in the HTCC process due to the high sintering temperature exceeding the melting point of other metals. This process results in higher strength but comes with the drawbacks of higher resistance and higher cost when compared with LTCC (Innovacera 2023). It may be possible to manufacture the sensor array and shield as a single unified block of HPA ceramic with this type of process, provided economic viability could be satisfied.

6.2 Frequency Analysis of IDC and CPC sensors

The CPC sensor frequency results (figure 15) show divergence of the water and methylated spirits samples occurring between ~ 10 kHz and ~ 200 kHz. From ~ 200 kHz to ~ 10 MHz the permittivity group demonstrate stable responses with Δf . In this frequency range, an increase in ϵ_r of the sample results in an increase in magnitude of the output, suggesting permittivity characterization is likely possible. Above ~ 10 MHz, stability begins to break down as the influence of the pole of the HPF diminishes and f approaches f_{cutoff} of the samples. The frequency response of ϵ shown in figure 8 of this report suggests this stability would likely continue past the breakdown point shown in this data if a HPF with a higher f_{cutoff} was used for the test. The ionic group show no discernible divergence for any NaCl concentration at any frequency. This feature renders the dual sensing approach described by Escriba et al unimplementable with this sensor. This is considered a negative feature of these results as the ability to measure ionic characteristics of soil at low frequency is considered a likely source of useful input signals for soil type classification models.

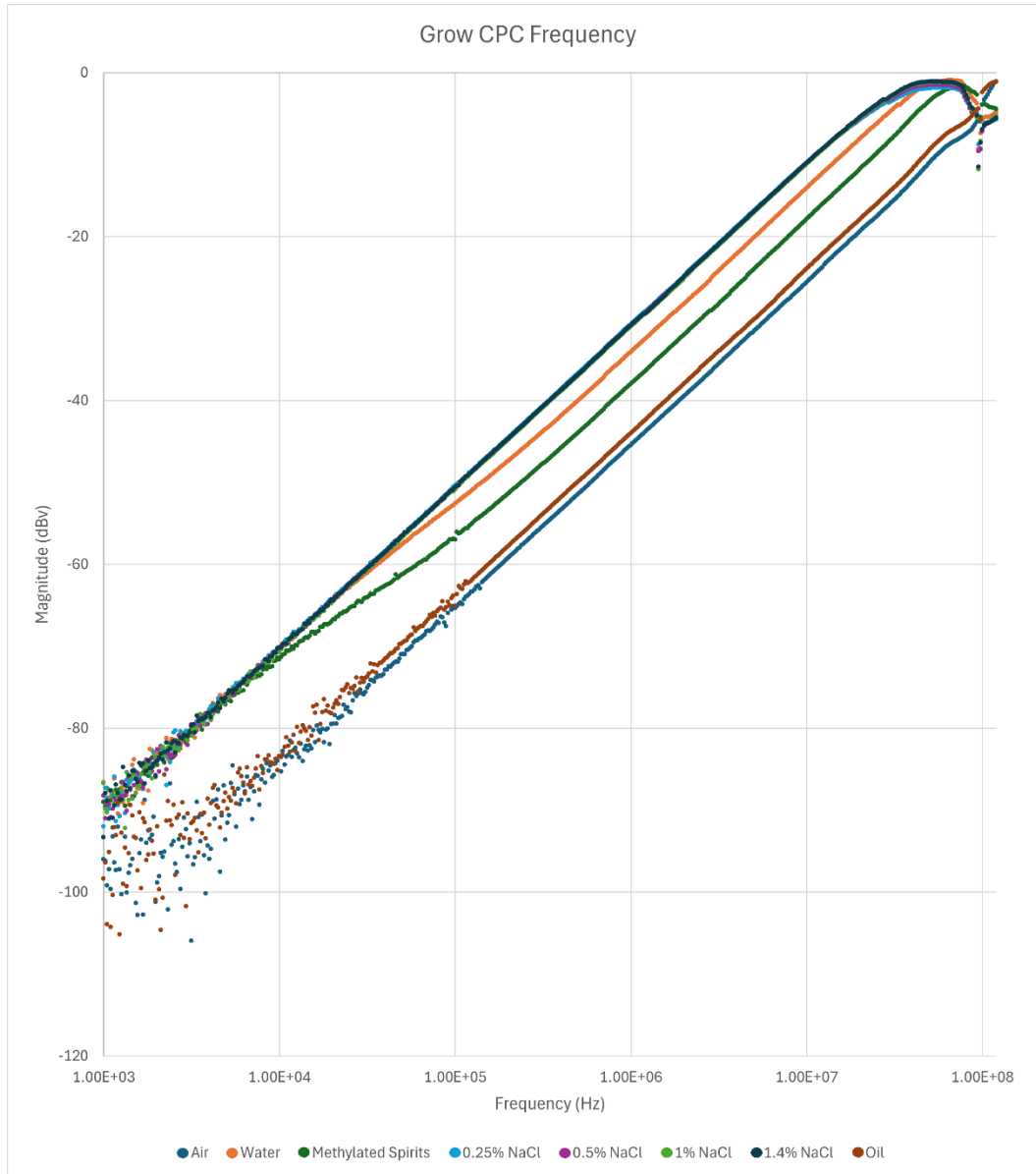


Figure 15: Grow CPC Sensor Frequency Plot.

The IDC sensor results (figure 16) show a transition from an ionic mode towards a dipolar mode of polarization of the MUT centred between 10 kHz and 100 kHz. This feature of the data is highly correlated with the relationship described in figure 8 of this report. Divergence of the water and methylated spirits samples occurs between ~20 kHz and ~800 kHz. Once divergence is complete, a larger sample ϵ_r results in a higher magnitude. The stability seen in the CPC frequency data (figure 15) is much less evident in this dataset due to the higher capacitances of the sensor lowering f_{cutoff} of the samples, it is likely this frequency stability continues to higher frequencies. The divergence of the NaCl datasets below ~10 kHz could enable characterisation of soil parameters such as conductivity and ionic content if the approach of dual frequency characterization demonstrated by Escriba et al were to be implemented in this work.

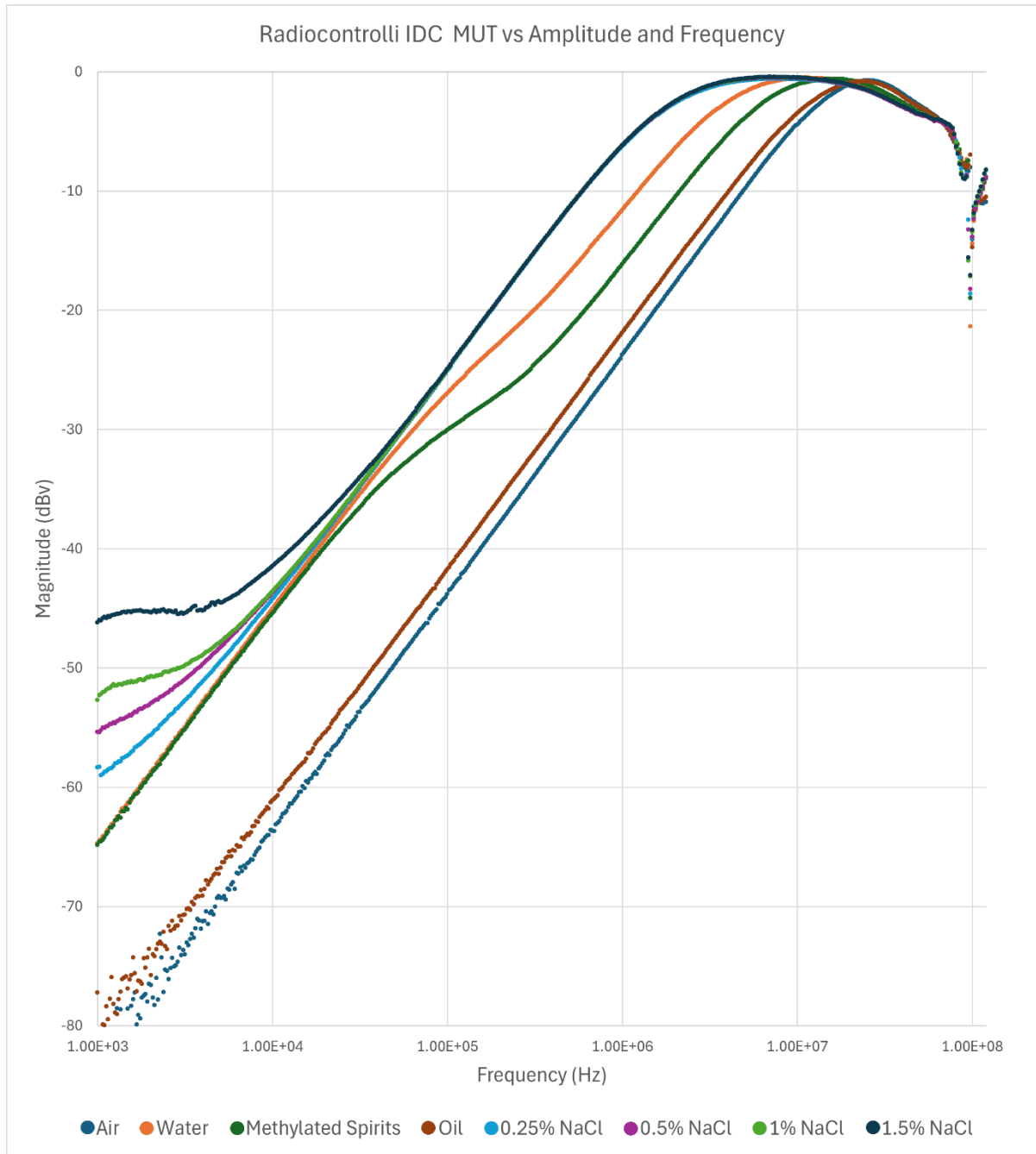


Figure 16: Radiocontrolli IDC Sensor Frequency Plot

A DMM was used to measure the bounds of capacitance of both sensors using the air (lowest) and 1.5% NaCl solution (highest) test samples.

	Radiocontrolli IDC sensor	Grow CPC sensor
Air	110pF	35pF
Submerged in 1.5% NaCl solution	1600pF	80pF

Table 2: Sensor capacitance values in air and distilled water.

The larger capacitance range for the IDC sensor of 110-1600pF compared to the CPC sensor range of 35-80pF represents a large increase in the overall dynamic range of the sensor. It was noticed during testing that the low capacitance value of the CPC sensor led to instability in readings if there was any movement in the test fixture. This would likely lead to unreliable sensor output in the mechanically aggressive working environment. Maximizing both the lower bound and range of sensor capacitance would be beneficial to future designs. The frequency analysis showed the divergence of the permittivity group was complete by ~ 1 MHz for both sensors. Figure 8 shows the minima for the ϵ'' component occurring between 10 MHz and 100 MHz. An excitation frequency in this 10-100 MHz band is likely to be optimal for moisture measurement.

6.3 Substrate Penetration

Figure 17 shows the results of penetration testing into distilled water through the 1mm substrate in brown alongside the submersion in distilled water dataset in blue and the air dataset in yellow. It is clear from these results that this sensor is incapable of penetrating the substrate into the MUT, as the substrate dataset is effectively equal to the air dataset.

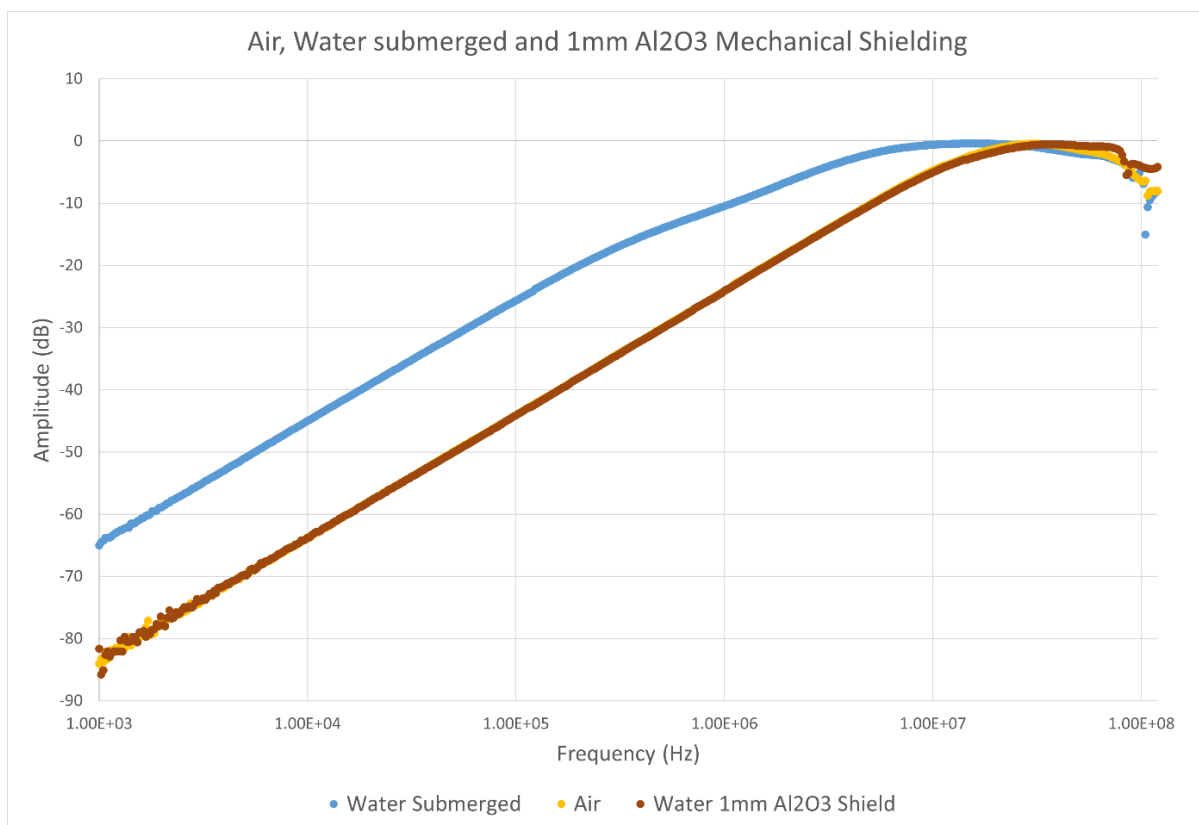


Figure 17: Result of IDC Al₂O₃ substrate penetration testing.

Figure 18 shows the results of substrate penetration testing performed on the CPC sensor. This test displays promising results for signal retention, displaying an acceptable drop in magnitude with the shield in place due to the parasitic capacitance introduced by the shield. For this sensor there were additional layers of FR4 PCB substrate and silkscreen that had to be penetrated as the sensor is constructed on the inner 2 copper layers of a 4-layer PCB. This test was performed twice, the first set of results lost almost all signal above ~30 kHz. In the second test, it was found that placing a blank PCB over the rear of the sensor as a ground plane greatly improved the outcome of the test. The fringing field of this sensor extends out from both the front and rear, the addition of this ground plane negates signal noise from the rear side. The IDC penetration test was rerun with this modification but demonstrated no discernible improvement.

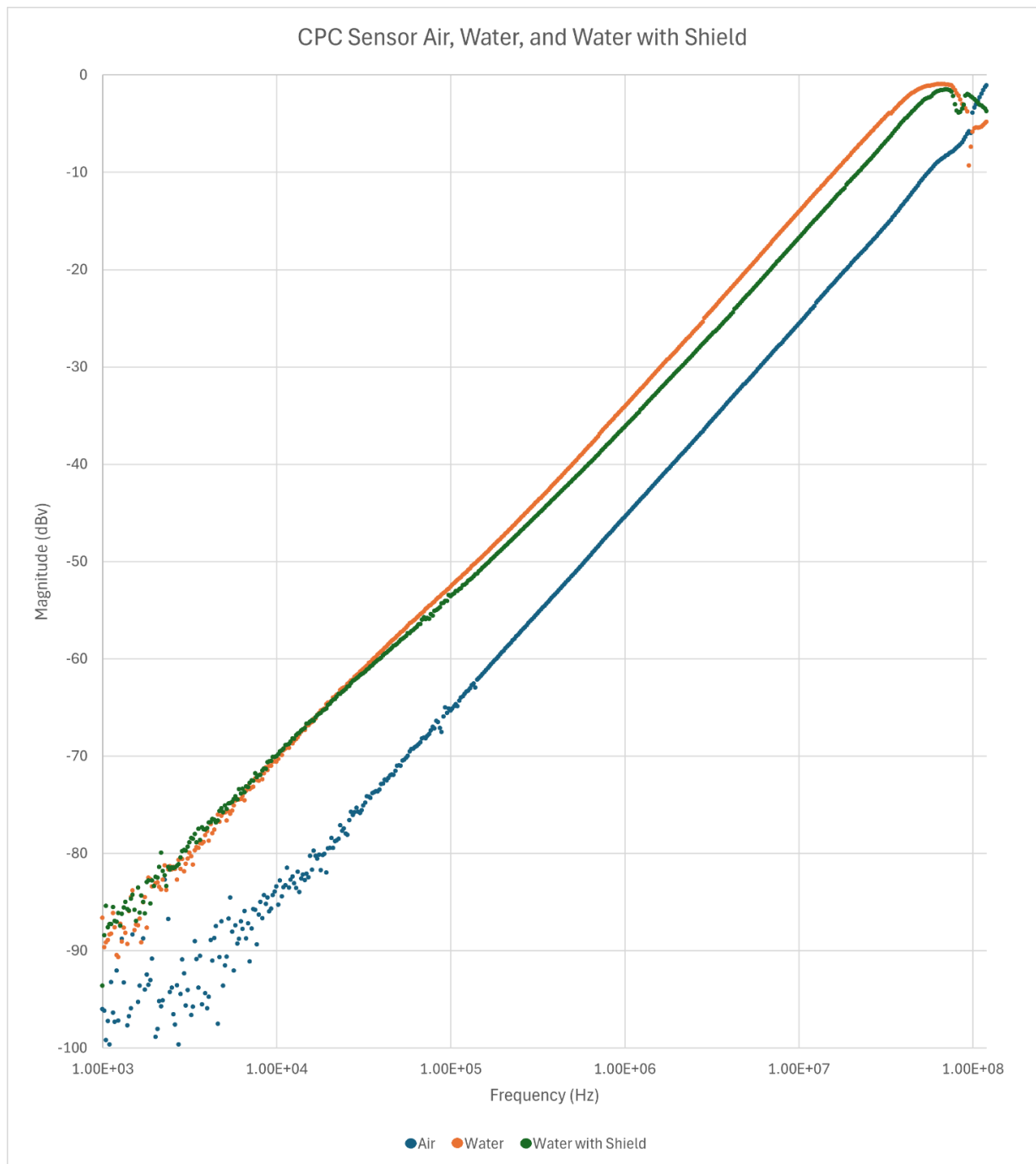


Figure 18: Result of CPC Al₂O₃ substrate penetration testing.

Although the IDC sensor failed to penetrate the alumina substrate, the configuration of this sensor was highly unsuited to this use-case. The sensor was designed for rain sensing applications with fine electrodes in very close proximity to the water droplets being measured. Claudel et al suggest penetration depth of IDC sensors is primarily a function of digit width and inter-digital gap width, so it is likely an IDC with digit dimensions optimized for this use-case may prove successful in this application (Claudel, et al. 2021). The use of ground planes for directing the fringing field greatly improved the shield penetration and sensitivity for the CPC sensor. Ground plane layouts should be tested and incorporated into future sensor designs. These results have identified the penetration of this mechanical shield layer as the most critical constraint on a design. To assist in dealing with this constraint, thinner substrates with a thickness of 0.64 mm and a higher purity of 99.5% Al_2O_3 have been sourced for use in future testing.

6.4 Characterization of IDC Sensor

An obvious linear relationship between ϵ_r and $V_{out\ pp}$ is present in the IDC characterization results (figure 19). The results demonstrate a $V_{out\ pp}$ dynamic range of 0.96v for air to 0.4v for water. The simulation in figure 14 shows this dynamic range can likely be optimized further with tuning of the excitation frequency if required. Small deviations are present in the water and methylated spirits mixtures, this is likely due to inaccuracies in volume measurements when creating these samples. The model fits the data very well overall, with an R^2 value of 0.9878.

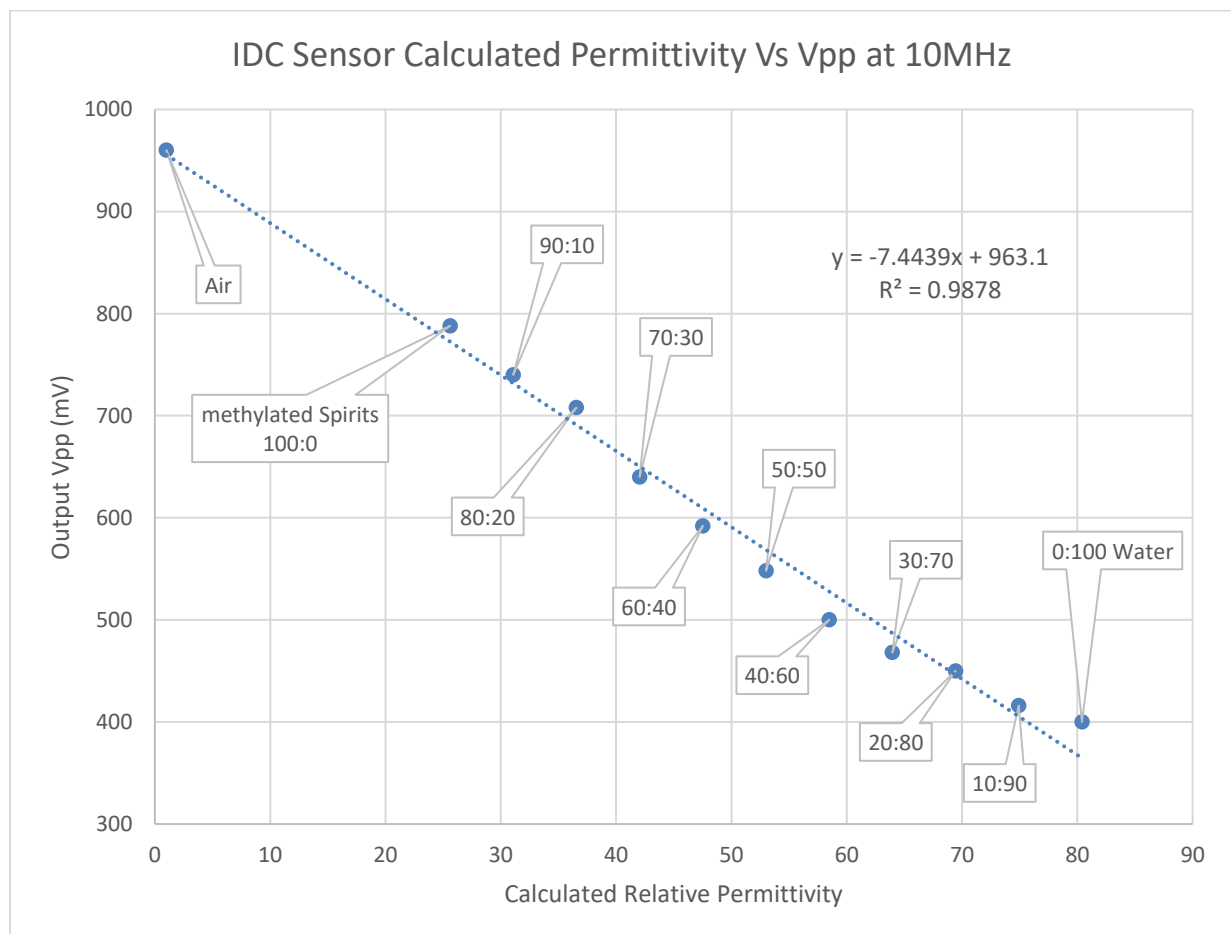


Figure 19: Radiocontrolli IDC Sensor Characterization Results.

Measuring only the amplitude of the output is a major limitation of this method in the presented form. This has proved effective in this testing, but the imaginary component ϵ_r'' has intentionally been minimized for this test. A much more useful characterization would also measure the phase shift of the output. This would require the sensor output signal to be compared to the sensor input signal and both ΔV_{pp} and the time delay between the signals to be measured.

To improve the outcome of this characterization method for a future sensor design the following alterations are suggested:

1. Comparing input and output signals could provide much more useful characterization across a wider range of materials as both the real and imaginary components of ϵ_r could be characterized.
2. The method will lack datapoints between $\epsilon_{r\ air}$ and the relative permittivity of the solute used. A solute which is miscible in water and has a low relative permittivity will allow better low-end characterization of the relationship. Examination of the tables in appendices F and G of this report suggest acetic acid may be a suitable solute, with an ϵ_r of 6.15, provided the low pH of an acid does not skew results.
3. Methylated spirits should be replaced with high purity solute to remove the uncertainty introduced by solute constitution.
4. Solutions should be created using molar concentration in place of the volumetric measurement method used in this work.
5. Characterization should be performed over a larger sample size.
6. This characterization should be performed with the mechanical shield in place.

7. Future Work

7.1 Plan of Approach for Future Development

To move the project forward, a sensor design targeting the specific requirements of this application must be created. The critical sensor characteristics identified during this testing of the ability to penetrate the shield layer, high minimum capacitance, high range of capacitance, an excitation frequency in the 10-100 MHz band, the use of ground planes to directing fringing fields, and high alumina purity of the shield layer should be targeted for optimization throughout this design process. The two sensors tested in this work were selected because they have vastly different designs, and this testing has demonstrated there are positive and negative aspects of both for this use-case. It is likely an optimal design sits somewhere in between.

To deal with the unique requirements of this application, sensor design optimization would likely best be performed with software modelling. Claudel et al validated the analytical method presented in that work using finite element analysis performed with the COMSOL Multiphysics software suite (Claudel, et al. 2021). Simulation and design optimization in this software is the logical next step for this research.

Once an optimal design has been identified from the software modelling, Gerber files of the design must be created. KiCad PCB design software is suggested for this step as it is freely available. Physical PCBs must then be manufactured from the Gerber files, a suitable manufacturer must be identified, and the physical boards must be sourced.

Upon receipt of physical PCBs, characterization of the sensor array can begin. The characterisation process has not been finalized, but the following characterization steps are suggested:

1. ϵ_r vs $V_{out\ pp}$ using the improved method suggested in section 6.4
2. Ionic characterization using low frequency oscillation source
3. Soil moisture percentage characterization in dry sand
4. Soil moisture percentage characterization in dry sand and variable levels of bentonite or kaolinite clay

7.1 Gantt Chart

Tasks	Pre-semester 2 2024							Semester 2 2024											
	10-Jun	17-Jun	24-Jun	1-Jul	8-Jul	15-Jul	22-Jul	29-Jul	5-Aug	12-Aug	19-Aug	26-Aug	2-Sep	9-Sep	16-Sep	23-Sep	30-Sep	7-Oct	14-Oct
Source COMSOL software																			
COMSOL FEA Modelling																			
PCB Design in KiCad																			
Source Physical PCBs																			
Permittivity characterization																			
Ionic characterization																			
Dry sand characterization																			
Clay characterization																			

8. References

- Accuratus. 2013. "Aluminium Oxide Ceramic Properties." <https://accuratus.com/https://accuratus.com/alumox.html>.
- Arcone, Steven, Steven Grant, Ginger Boitnott, and Benjamin Bostick. 2008. "Complex permittivity and clay mineralogy of grain-size fractions in a wet silt soil." *Geophysics* 73: J12. doi:10.1190/1.2890776.
- Ausplow. 2024. "SOIL HEALTH AN AGENDA ITEM." *Ausplow*. <https://www.ausplow.com.au/soil-health-an-agenda-item/>.
- Bodini, A, E Sardini, M Serpelloni, and S Pandini. 2018. "Novel Coplanar Capacitive Force Sensor for Biomedical Applications: A Preliminary Study. ." *Sensors* 329-336. doi:https://doi.org/10.1007/978-3-030-04324-7_41.
- China Alumina Ceramic. 2022. "ALUMINA CERAMIC PLATE." <https://www.aluminaceramicball.com/https://www.aluminaceramicball.com/product/alumina-ceramic-plate/>.
- Claudel, J, A L Alves de Araujo, D Kourtiche, M Nadi, and A Bourjilat. 2021. "Optimization of Interdigitated Sensor." *Interdigital Sensors* 36: 91-122. doi:https://doi.org/10.1007/978-3-030-62684-6_5.
- Congreve, Mark. 2022. *Paddock Practices: Dry sowing and pre-emergent herbicides*. GRDC. <https://grdc.com.au/resources-and-publications/all-publications/paddock-practices/2022/national/march/dry-sowing-and-pre-emergent-herbicides>.
- Dean, Robert N, Aditi Rane, Michael Baginski, Zane Hartzog, and David J Elton. 2010. "Capacitive fringing field sensors in printed circuit board technology." *2010 IEEE Instrumentation & Measurement Technology Conference Proceedings*. Austin, TX, USA: IEEE. 970-974. doi:10.1109/IMTC.2010.5488058.
- Department of Primary Industries. 2024. "Western Australian Crop Sowing Guide." 34-35.
- Disco Technology. n.d. "Co-fired Ceramics." <https://technology.discousa.com/https://technology.discousa.com/material/ceramics/#:~:text=HTCC%20is%20a%20ceramic%20based,is%20also%20called%20glass%20ceramics>.
- Dong, Xiaobo, and Yu-Hsing Wang. 2008. "The Effects of the pH-influenced Structure on the Dielectric Properties of Kaolinite–Water Mixtures." *Soil Physics* 72: 1532-1541. doi:10.2136/sssaj2007.0238.
- Electronics Tutorials. 2024. https://www.electronics-tutorials.ws/https://www.electronics-tutorials.ws/capacitor/cap_1.html.
- Escriba, Christophe, Eli Gabriel Avina Bravo, Julien Roux, Jean-Yves Fourniols, Michel Contardo, Pascal Acco, and Georges Soto-Romero. 2020. "Toward Smart Soil Sensing in v4.0 Agriculture: A New Single-Shape Sensor for Capacitive Moisture and Salinity Measurements." *Sensors* 20: 6867. doi:https://doi.org/10.3390/s20236867.
- Fernandez, Diego P, Y Mulev, A.R.H. Goodwin, and J.M.H. Levent Sengers. 1995. "A database for the static dielectric constant of water and steam." Thermophysics division, National Institute of Standards and Technology, Gaithersburg, 35. <https://www.nist.gov/document/jpcrd487pdf>.
- Finlay, David, and Gordon Howard. 2024. *Integrating soil moisture sensor technology into seeding equipment to optimise seeding depth and crop establishment*. Moisture Planting Technologies Pty Ltd, GRDC, 1-6. https://grdc.com.au/__data/assets/pdf_file/0032/597236/Paper-Finlay-David-2024.pdf.
- GDRC. 2016. "WHEAT PLANT GROWTH AND PHYSIOLOGY." 1-10. https://grdc.com.au/__data/assets/pdf_file/0028/373906/GrowNote-Wheat-South-04-Physiology.pdf.
- González, Gabriel, Eleazar Samuel Kolosovas-Machuca, Edgar López-Luna, Heber Hernández-Arriaga, and Francisco Javier González. 2015. "Design and Fabrication of

- Interdigital Nanocapacitors Coated with HfO₂.” *sensors* 15: 1998-2005.
doi:10.3390/s150101998.
- GRDC. n.d. “MANAGING SOIL WATER TO IMPROVE GRAIN PROFITS.” 1-6.
https://grdc.com.au/__data/assets/pdf_file/0036/287892/Managing-Soil-Water-Central-Queensland.pdf.
- . 2024. “Trials to dive deep into moisture-seeking wheats.”
<https://groundcover.grdc.com.au/>. <https://groundcover.grdc.com.au/crops/cereals/trials-to-dive-deep-into-moisture-seeking-wheats>.
2020. “Impact of sowing depth and seed size on the dynamics of germination and productivity of spring wheat.” *Polish Journal of Agronomy* 43: 63-69. doi:doi:10.26114/pja.iung.421.2020.43.06.
- Innovacera. 2023. “Do you know the difference between HTCC and LTCC?”
<https://www.innovacera.com/>. <https://www.innovacera.com/news/do-you-know-the-difference-between-htcc-and-ltcc.html>.
- Kim, Man-Il, Byung-Gon Chae, and Makoto Nishigaki. 2008. “Evaluation of geotechnical properties of saturated soil using dielectric responses.” *Geosciences* 83-93.
doi:10.1007/s12303-008-0010-0.
- Li, Chuanlan, Changying Wu, and Lifei Shen. 2022. “Complex Permittivity Measurement of Low-Loss Anisotropic Dielectric Materials at Hundreds of Megahertz.” *electronics* 11: 2. doi:<https://doi.org/10.3390/electronics11111769>.
- Li, Fangxin, Yangong Zheng, Changzhou Hau, and Jiawen Jian. 2019. “Gas Sensing by Microwave Transduction: Review of Progress and Challenges.” *Frontiers in Materials* 6: 4. doi:10.3389/fmats.2019.00101.
- Llewellyn, Rick, and Jackie Ouzman. 2020. “Conservation agriculture in Australia: 30 years on.” 22.
- MIT. n.d. “Capacitance and Dielectrics .” <https://web.mit.edu/>.
<https://web.mit.edu/8.02t/www/802TEAL3D/visualizations/coursenotes/modules/guide05.pdf>.
- Nguyen, Manh Duc, Romulus Costache, An Ho Sy, Hassan Ahmadzadeh, Hiep Van Le, Indra Prakash, and Binh Thai Pham. 2022. “Novel approach for soil classification using machine learning methods.” *Bulletin of Engineering Geology and the Environment* 81 (468): 1-17. doi:<https://doi.org/10.1007/s10064-022-02967-7>.
- Oregon State University. 2024. “Germination and Seedling Emergence.”
<https://forages.oregonstate.edu/>. <https://forages.oregonstate.edu/regrowth/how-does-grass-grow/developmental-phases/vegetative-phase/germination-and-seedling>.
- Oyeniran, Oyedotun Kabir. 2018. “Synthesis and characterization of carbon-based nanostructured material electrodes for designing novel hybrid supercapacitors.” PhD Thesis, Faculty of Natural and Agricultural Sciences, University of Pretoria.
doi:10.13140/RG.2.2.20007.50084.
- Patle, Kamlesh S, Vishvesh Panchal, Riya Saini, Yash Agrawal, and Vinay S Palaparthi. 2022. “Temperature compensated and soil density calibrated soil moisture.” *Measurements* 201: 111703. doi:<https://doi.org/10.1016/j.measurement.2022.111703>.
- Pumpa, Jennifer, Peter Martin, Frank McRae, and Neil Coombes. 2013. “Coleoptile length of wheat varieties.” NSW Department of Primary Industries, 1-5.
https://www.dpi.nsw.gov.au/__data/assets/pdf_file/0006/459006/Coleoptile-length-of-wheat-varieties.pdf.
- Radiocontrolli. n.d. “RC-SPC1K Rain Sensor Datasheet.” <https://www.radiocontrolli.com/>.
https://www.radiocontrolli.com/media/1327_19f7fbdeee533922c0340d47b898e025e70c0574.pdf/o/RC-SPC1K.pdf.
- RecoChem. 2022. “Diggers methylated spirits safety data sheet.” www.recochem.com.
<https://www.recochem.com>.

- Rêgo Segundo, A.K., É. Silva Pinto, G Almeida Santos, and P.M. de Barros Monteiro. 2019. "Capacitive Impedance Measurement: Dual-frequency Approach." *Sensors* 19: 1-12. doi:<https://doi.org/10.3390/s19112539>.
- Sigma-Aldrich. 2024. "Solvent Miscibility Table." www.sigmaaldrich.com.
<https://www.sigmaaldrich.com/AU/en/technical-documents/technical-article/analytical-chemistry/purification/solvent-miscibility-table>.
- Sulek, Alicja, and Monika Ogorkiewicz. 2020. "Impact of sowing depth and seed size on the dynamics of germination and productivity of spring wheat." *Polish Journal of Agronomy* 43: 63-69. doi:doi: 10.26114/pja.iung.421.2020.43.06.
- Topp, G.C., D.R. Lapen, G.D. Young, and M. Edwards. n.d. "EVALUATION OF SHAFT-MOUNTED TDT READINGS IN DISTURBED AND UNDISTURBED MEDIA." https://www.researchgate.net/publication/267924009_EVALUATION_OF_SHAFT-MOUNTED_TDT_READINGS_IN_DISTURBED_AND_UNDISTURBED_MEDIA.
- University of Washington. n.d. "Dielectric constants of Common Solvents." *UW Departments Web Server*.
https://depts.washington.edu/eoopic/linkfiles/dielectric_chart%5B1%5D.pdf.
- Yang, Yang, Thomas Vervust, Frederick Bossuyt, Jan Vanfleteren, Gabriele Chiesura, Geert Luyckx, Joris Degrieck, and Markus Kaufmann. 2015. "Non-destructive evaluation of an infusion process using capacitive sensing technique." In *Emerging Technologies in Non-Destructive Testing VI*, 293-297. <https://core.ac.uk/download/pdf/55781827.pdf>.
- Yu, Limin, Wanlin Gao, Redmond R Shamshiri, Sha Tao, Yanzhao Ren, Yanjun Zhang, and Guilian Su. 2021. "Review of research progress on soil moisture sensor technology." *International Journal of Agricultural and Biological Engineering* 32-42. doi:10.25165/j.ijabe.20211404.6404.
- Zareian, A, A Hamidi, H Sadeghi, and M.R. Jazaeri. 2013. "Effect of Seed Size on Some Germination Characteristics, Seedling Emergence Percentage and Yield of Three Wheat (*Triticum aestivum* L.) Cultivars in Laboratory and Field." *Middle-East Journal of Scientific Research* 13 (8): 1126-1131. doi:10.5829/idosi.mejsr.2013.13.8.651.

Appendix A: Coleoptile Length Classification of Certain Wheat Varieties

Figure 18 shows data from a field trial conducted in 2021 comparing coleoptile length, seedling establishment and yield results at 0, 4 and 10 cm sowing depths over a range of wheat varieties. Figure 19 show a list of wheat varieties and their coleoptile group classifications (Department of Primary Industries 2024).

Variety (Coleoptile group)	Coleoptile length (cm)		Establishment (m ²) at 10cm deep	Grain yield (t/ha)	
	Filter paper	Sown at 10cm		at 10cm deep	at 4cm deep
DS Pascal (S)	6.3	4.9	27	2.3	4.4
Scepter (S/M)	7.5	5.5	31	2.5	5.0
Calibre (L)	8.5	6.7	48	3.0	4.9
Yitpi (L)	9.4	6.8	58	2.7	4.6
Halberd (VL)	12.3	7.8	100	3.3	4.2
Isd			30 (m ²)	0.5 (t/ha)	0.5 (t/ha)

Figure 20: Coleoptile length, establishment rate, and yield of a range of wheat varieties at 0, 4 and 10 cm sowing depth.

Variety	Black point [†]	Falling number index	Coleoptile group
Brumby	MSp	6p	M
Calibre	MSp	6p	L
Catapult	S	6	M
Chief CL Plus	MS	4	M
Cutlass	MS	4	L
Denison	MS	5	M/L
Devil	MSS	3	M
DS Bennett	MSS	-	M
DS Pascal	MS	7	S
Hammer CL Plus	MRMS	4	M
Illabo	MRMS	5	M
Kinsei	S	4	M
LRPB Anvil CL Plus	Sp	2/3p	M
LRPB Avenger	MS	5p	-
LRPB Havoc	MS	3	-
LRBP Nighthawk	MS	-	-
LRPB Trojan	MS	5	-
Mace	MRMS	5	M
Magenta	MSS	3	L
Mowhawk	-	5	Mp
Ninja	MRMS*	4	S/M
Razor CL Plus	MS	4	M
Rockstar	MSS	2	M
Scepter	MS	5	S/M
Sheriff CL Plus	MS	4	-
Sting	S	4p	M/L
Valiant CL Plus	MSp	2/3p	M
Vixen	MSS	3	M
Westonia	MS*	2	M
Wyalkatchem	MS*	3	S
Yitpi	MS	5	L
Zen	MRMS	3	S

Figure 21: List of wheat varieties and their coleoptile group classifications.

Appendix B: Soil Classification Correlation Matrix

Figures 22 and 23 show the features used for soil type classification and the correlation matrix between them in Nguyen et al.

STT	Features	Description	Maximum	Minimum	Mean	Standard deviation
1	X1	Soil sample	93.7	0.4	23.4	16.58
2	X2	Lower depth of soil sample	94	1	23.81	16.48
3	X3	Clay content	70.79	0.5	22.3	9.74
4	X4	Silt content	92.7	4.5	39.93	17.95
5	X5	Liquid limit	98.14	19.68	47.24	10.95
6	X6	Plastic limit	53.39	3	25.68	5.1
7	X7	Plastic index	66.07	3.3	21.57	8.26
8	X8	Liquidity index	4.11	0.01	0.67	0.39
9	X9	Water content	120.2	12.22	39.25	11.49
10	X10	Wet density	2.22	1.22	1.8	0.12
11	X11	Dry density	1.93	0.57	1.31	0.19
12	X12	Specific gravity	2.87	2.53	2.69	0.03
13	X13	porosity	78.89	29.03	51.36	6.92
14	X14	Degree of saturation	100	38	95.76	3.78
15	X15	Void ratio	3.74	0.41	1.1	0.31

Figure 22: Soil Classification Features used for Model Evaluation. From: (Nguyen, et al. 2022).

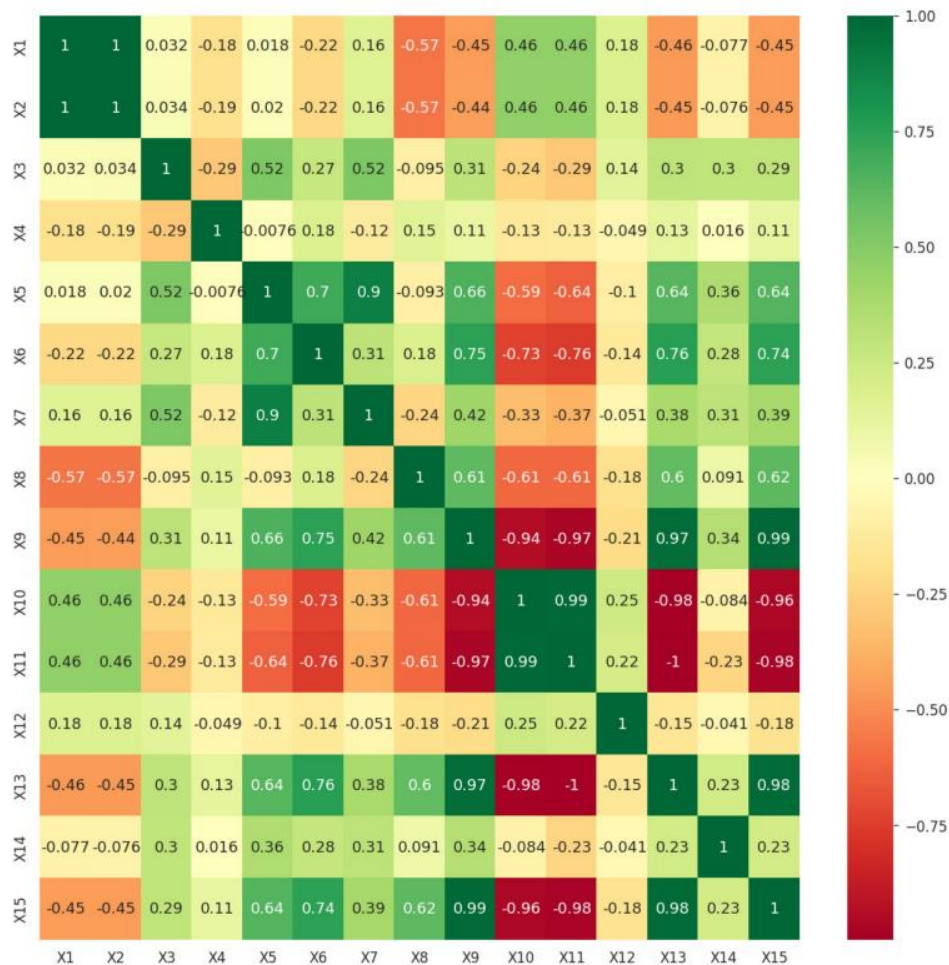


Figure 23: Correlation Matrix of Soil Parameters. From: (Nguyen, et al. 2022).

Appendix C: Deviation of Method Described by Rego Segunda et al

Rego Segundo et al demonstrate the following method for complex admittance approximation (Rêgo Segundo, et al. 2019):

$$\epsilon_r = \epsilon_r' - j \frac{\sigma}{\omega \epsilon_0} \quad (11)$$

Ohms law for AC circuits states:

$$\mathbf{V} = \mathbf{Z}\mathbf{I} \quad (12)$$

Where \mathbf{V} and \mathbf{I} are the AC voltage and current phasors respectively and \mathbf{Z} is the complex impedance:

$$\mathbf{Z} = R + jX \quad (13)$$

Where R is resistance and X is reactance in Ohms. The admittance \mathbf{Y} is the inverse of \mathbf{Z} :

$$\mathbf{Z}^{-1} = \mathbf{Y} = G + jB \quad (14)$$

Where G is conductance and B is the susceptance in Siemens. Both G and B are dependent on the geometric configuration constant of the sensor k_g , (i.e. for the simple PPC case in equation 2, $k_g = \frac{A}{d}$) and:

$$G = k_g \sigma, \quad B = k_g \omega \epsilon_0 \epsilon_r' \quad (15)$$

$$\mathbf{Y} = k_g \sigma + j k_g \omega \epsilon_0 \epsilon_r' \quad (16)$$

Taking out the factor $j k_g \omega \epsilon_0$ from equation 16:

$$\mathbf{Y} = j k_g \omega \epsilon_0 \left(\frac{\sigma}{j \omega \epsilon_0} + \epsilon_r' \right) \quad (17)$$

Simplifying the imaginary denominator:

$$\mathbf{Y} = j k_g \omega \epsilon_0 \left(\frac{\sigma(-j \omega \epsilon_0)}{j \omega \epsilon_0 (-j \omega \epsilon_0)} + \epsilon_r' \right) = j k_g \omega \epsilon_0 \left(\frac{\sigma(-j \omega \epsilon_0)}{-j^2 \omega^2 \epsilon_0^2} + \epsilon_r' \right) \quad (18)$$

$$\mathbf{Y} = j k_g \omega \epsilon_0 \left(-j \frac{\sigma}{\omega \epsilon_0} + \epsilon_r' \right) \quad (19)$$

Using equation 11 in equation 19:

$$\therefore \mathbf{Y} = j k_g \omega \epsilon_0 \epsilon_r \quad (20)$$

Appendix D: Methylated Spirits Composition and Uncertainty Calculations

SECTION 3 COMPOSITION AND INFORMATION ON INGREDIENTS		
Ingredients Names and Proportions		
Chemical Entity	CAS Number	Proportion (%)
Ethanol	64-17-5	>= 95
Demin. Water	7732-18-5	<= 5
The following materials make up the denaturant of the fluid. They are not present in high enough concentrations to trigger any additional hazards.		
Denatonium Benzoate	3734-33-6	< 0.001
Methyl Isobutyl Ketone	108-10-1	0.25
Fluorescein	-	< 0.001

Figure 24: Methylated Spirits Composition. From: (RecoChem 2022).

Table 1: Relative dielectric permittivity of liquids		
Medium	Reference ϵ_r	$\sqrt{\epsilon_r}$
Cyclohexane	2.02	1.42
Benzene	2.27	1.51
Amyl acetate	4.75	2.18
Ethyl acetate	6.02	2.45
1-octanol	10.34	3.22
2-butanol	16.56	4.07
1-butanol	17.51	4.18
2-propanol	19.82	4.45
Ethanol	24.6	4.96
Ethanol:water (2:1)	43.2	6.57
Ethanol:water (1:1)	52.5	7.25
Ethanol:water (1:3)	66.45	8.15
Water	80.4	8.97

Figure 25: Relative Permittivity Values used for Characterization. From: (Topp, et al. n.d.).

$$95\% \times \epsilon_{r \text{ Ethanol}} + 5\% \times \epsilon_{r \text{ water}} = 27.39,$$

$$\text{Mean} = \frac{27.39 + 24.6}{2} \approx 25.6,$$

$$\text{Uncertainty of } \epsilon_r \text{ for methylated spirits} = \frac{27.39 - 24.6}{2} \approx 1.4, \approx \pm 5.47\%$$

Appendix E: Complex Permittivity of Ethanol vs Frequency

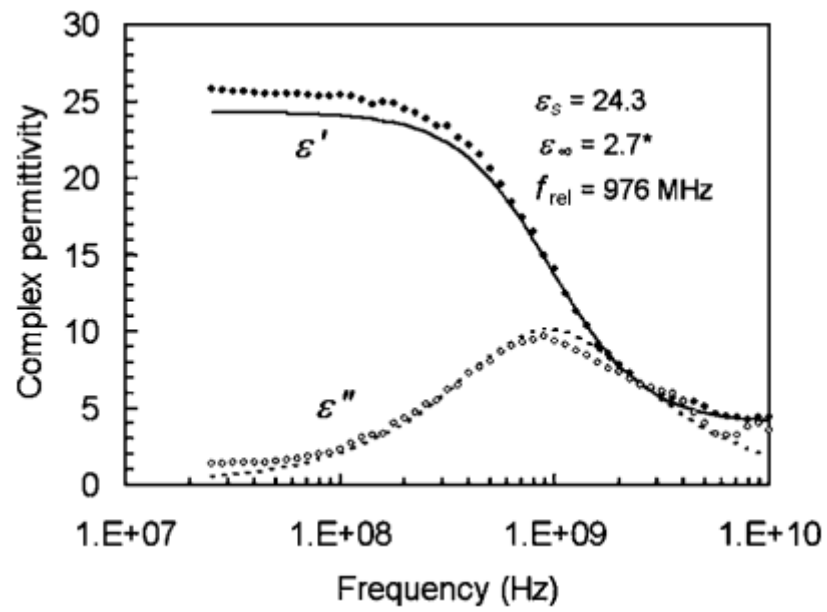


Figure 26: Complex Permittivity of Ethanol vs Frequency. From: (Arcone, et al. 2008).

Appendix F: Water Miscibility Chart

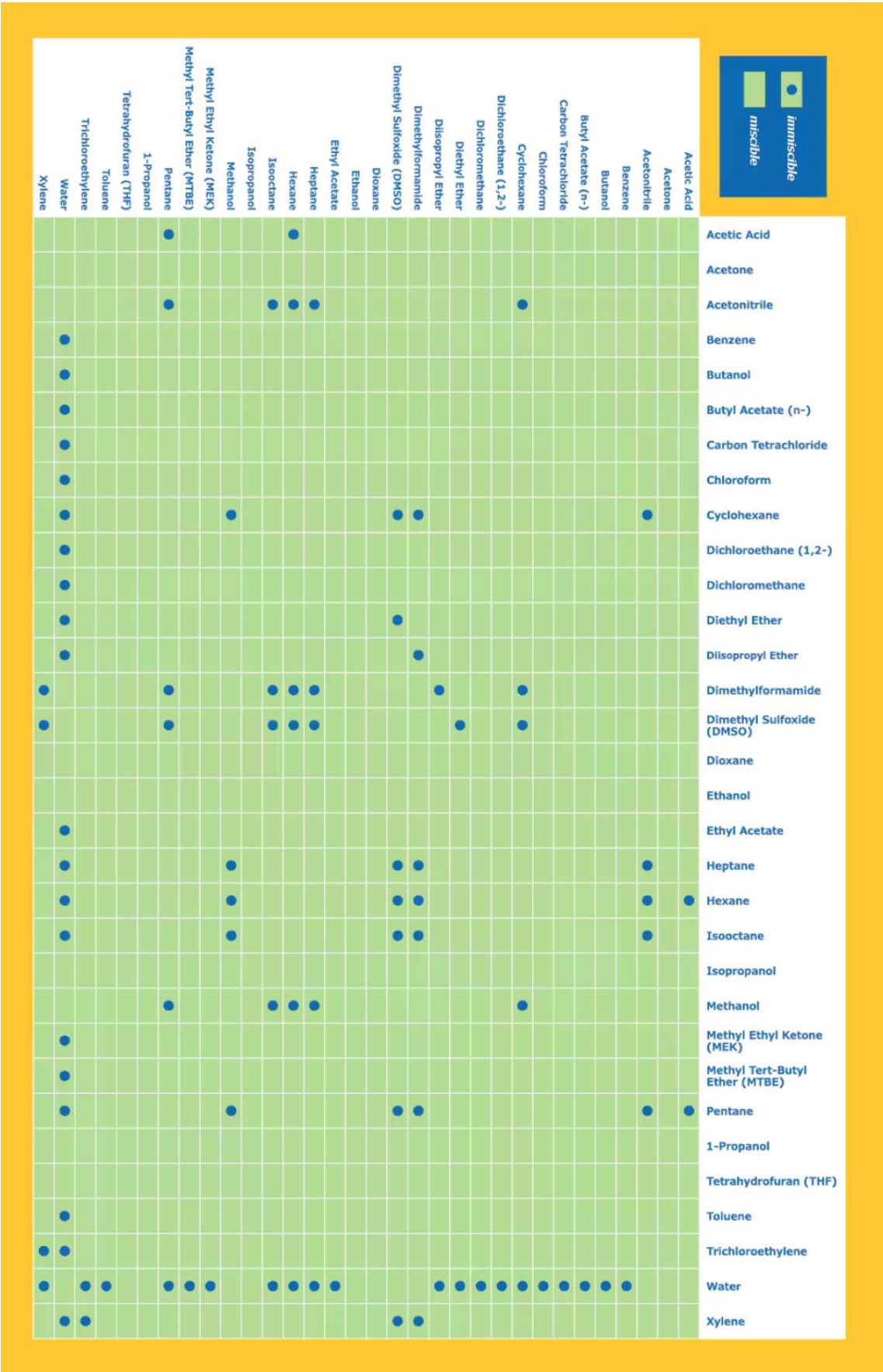


Figure 27: Water Miscibility Chart. From: (Sigma-Aldrich 2024)

Appendix G: Dielectric Constant of Common Solvents

Solvent	mp	bp	D_4^{20}	n_D^{20}	ϵ	R_D	μ
Acetic acid	17	118	1.049	1.3716	6.15	12.9	1.68
Acetone	-95	56	0.788	1.3587	20.7	16.2	2.85
Acetonitrile	-44	82	0.782	1.3441	37.5	11.1	3.45
Anisole	-3	154	0.994	1.517	4.33	33	1.38
Benzene	5	80	0.879	1.5011	2.27	26.2	0
Bromobenzene	-31	156	1.495	1.558	5.17	33.7	1.55
Carbon disulfide	-112	46	1.274	1.6295	2.6	21.3	0
Carbon tetrachloride	-23	77	1.594	1.4601	2.24	25.8	0
Chlorobenzene	-46	132	1.106	1.5248	5.62	31.2	1.54
Chloroform	-64	61	1.489	1.4458	4.81	21	1.15
Cyclohexane	6	81	0.778	1.4262	2.02	27.7	0
Dibutyl ether	-98	142	0.769	1.3992	3.1	40.8	1.18
<i>o</i> -Dichlorobenzene	-17	181	1.306	1.5514	9.93	35.9	2.27
1,2-Dichloroethane	-36	84	1.253	1.4448	10.36	21	1.86
Dichloromethane	-95	40	1.326	1.4241	8.93	16	1.55
Diethylamine	-50	56	0.707	1.3864	3.6	24.3	0.92
Diethyl ether	-117	35	0.713	1.3524	4.33	22.1	1.3
1,2-Dimethoxyethane	-68	85	0.863	1.3796	7.2	24.1	1.71
<i>N,N</i> -Dimethylacetamide	-20	166	0.937	1.4384	37.8	24.2	3.72
<i>N,N</i> -Dimethylformamide	-60	152	0.945	1.4305	36.7	19.9	3.86
Dimethyl sulfoxide	19	189	1.096	1.4783	46.7	20.1	3.9
1,4-Dioxane	12	101	1.034	1.4224	2.25	21.6	0.45
Ethanol	-114	78	0.789	1.3614	24.5	12.8	1.69
Ethyl acetate	-84	77	0.901	1.3724	6.02	22.3	1.88
Ethyl benzoate	-35	213	1.05	1.5052	6.02	42.5	2
Formamide	3	211	1.133	1.4475	111	10.6	3.37
Hexamethylphosphoramide	7	235	1.027	1.4588	30	47.7	5.54
Isopropyl alcohol	-90	82	0.786	1.3772	17.9	17.5	1.66
Methanol	-98	65	0.791	1.3284	32.7	8.2	1.7
2-Methyl-2-propanol	26	82	0.786	1.3877	10.9	22.2	1.66
Nitrobenzene	6	211	1.204	1.5562	34.82	32.7	4.02
Nitromethane	-28	101	1.137	1.3817	35.87	12.5	3.54
Pyridine	-42	115	0.983	1.5102	12.4	24.1	2.37
Tetrahydrofuran	-109	66	0.888	1.4072	7.58	19.9	1.75
Toluene	-95	111	0.867	1.4969	2.38	31.1	0.43
Trichloroethylene	-86	87	1.465	1.4767	3.4	25.5	0.81
Triethylamine	-115	90	0.726	1.401	2.42	33.1	0.87
Trifluoroacetic acid	-15	72	1.489	1.285	8.55	13.7	2.26
2,2,2-Trifluoroethanol	-44	77	1.384	1.291	8.55	12.4	2.52
Water	0	100	0.998	1.333	80.1	3.7	1.82
<i>o</i> -Xylene	-25	144	0.88	1.5054	2.57	35.8	0.62

Figure 28: Permittivity of Common Solvents. From: (University of Washington n.d.).